Search for Wt-channel single top quark production in 7 TeV proton-proton collisions using the ATLAS detector

by

Dominique Tardif

A thesis submitted in conformity with the requirements
for the degree of Doctor of Philosophy
Graduate Department of Physics
University of Toronto

Abstract

Search for Wt-channel single top quark production in 7 TeV proton-proton collisions using the ATLAS detector

Dominique Tardif

Doctor of Philosophy

Graduate Department of Physics

University of Toronto

2011

The production of single top quarks through the weak interaction is of great interest in particle physics, as it provides the only means to directly measure the CKM matrix element $|V_{tb}|$, one of the few remaining Standard Model parameters which has yet to be precisely constrained by direct experimental measurements. This thesis describes a search for Wt-channel single top quark production using proton-proton collision data collected at a center-of-mass energy of 7 TeV by the ATLAS detector at the Large Hadron Collider, corresponding to a total integrated luminosity of 35 pb^{-1}. Collision events having exactly two oppositely-charged electrons or muons, a single high-transverse-momentum jet, and large missing or total transverse energy are selected, resulting in a sample with enhanced single top purity. 38 data events are found to survive the selection, in good agreement with the expected sum from all signal and background predictions of 38.6 ± 6.0. The Wt content of the selected sample is predicted to amount to 4.3 ± 0.3 events. The resulting cross-section measurement is

$$\sigma(pp \to Wt) = 10\ ^{+20}_{-10}\,(\text{stat})\ ^{+20}_{-10}\,(\text{syst})\ \text{pb}.$$

As this level of precision is insufficient to claim evidence or discovery of this process, an upper limit is also derived for the parameter of interest, resulting in $\sigma(pp \to Wt) < 70$ pb at 95% confidence level.

Acknowledgements

First and foremost, words cannot convey the depth of my gratitude to my wife Hanako for her love, support, patience, and understanding, particularly over the last two years. I can always count on you, Mai and Pūchan to brighten my day and remind me about the important things in life.

I would like to thank my parents, René and Carole, for always nurturing my interest in math and science and encouraging me to pursue a higher education. Thanks to Pancha and Mancha for their infectious joie de vivre.

I am immensely grateful to my supervisor, Professor William Trischuk, for his flexibility, his unwavering support, and for sharing his in-depth knowledge of experimental high-energy physics. Thanks also to my doctoral committee members, Professors Michael Luke and Barth Netterfield, for their time and valuable insights.

I am indebted to my colleagues in the ATLAS Beam Conditions Monitor, top cross-section, and single top groups. Daniel Dobos, Matthew Fisher, Andrej Gorišek, Boštjan Maček, and Marko Mikuž were all very nice and helpful at one time or another. Thanks to Arnaud Lucotte for taking a chance on me when I was starting out in ATLAS and wanted to work on single top. Thanks to Arnaud as well as Julien Donini, Reinhard Schwienhorst, and Wolfgang Wagner for their hard work and patience in dealing with a rookie co-editor during the approval process for the winter conferences. Thanks to Kyle Cranmer for his willingness to share his statistical expertise.

Thanks to my officemates in Toronto, Sing Leung Cheung, Pier-Olivier DeViveiros, Bin Guo, and Trevor Stewart, for their friendship.

I gratefully acknowledge the financial support of the Natural Science and Engineering Research Council of Canada, E. C. Stevens, Cray Inc., and the University of Toronto.

Finally, thanks to the operators of Kohina for providing the musical background to most of my productive working hours in the past few years.

Contents

List of Tables

List of Figures

Chapter 1

Introduction

Ever since Democritus famously posited that "the first principles of the universe are atoms and empty space", the idea that all observable matter is built up from a set of indivisible, fundamental particles has been one of the tenets of science. The quest for these fundamental constituents only became possible after the scientific and technological breakthroughs of the Enlightenment, resulting in the elements of Lavoisier and the later discovery of atomic substructure. The Standard Model of particle physics, a theory developed in the 1960's, represents the latest development in this 2,500-year-old endeavour. According to the Standard Model, all matter is composed of only twelve flavours of quarks and leptons that interact by exchanging four types of force-carrying particles. One last particle, the Higgs boson, gives mass to the quarks and leptons, but it has yet to be observed in experiments. The Standard Model has been an extraordinarily successful theory, providing accurate predictions for the results of particle physics experiments for nearly fifty years. However, it is also known to be incomplete, as it suffers from a number of theoretical issues at very high energies.

The top quark was one of the the last Standard Model particles to be experimentally observed; this was finally achieved in 1995 by the CDF [1] and D0 [2] collaborations. In the 16 years since, experimental high-energy physicists have been hard at work studying its properties and interactions. These efforts have yielded a number of interesting results: for example, the top quark's mass has been measured to be 172.0 ± 1.6 GeV, which makes it more than 40 times heavier than any other fundamental fermion. The Standard Model provides no explanation for this bizarre mass hierarchy, and it is hoped that detailed studies of the top quark's properties may help solve the mystery. Already, tentative signs are emerging: the CDF collaboration recently published evidence of a mass-dependent forward-backward asymmetry in top quark pair production which is much larger than the Standard Model prediction [3]. This could be one of the first clear manifestations of physics beyond the Standard Model, and further reinforces the point that top quark studies are extremely important for the future of particle physics.

In hadron collisions, top quarks are most often produced as top-antitop pairs through the strong interaction. The production of single top quarks through the electroweak interaction is also possible and proceeds through three processes, known as t-channel, Wt-channel, and s-channel, with distinct production rates and phenomenological characteristics. Though rarer than top pair production, single top production is arguably more interesting from a theoretical perspective, as it provides the only opportunity for direct measurements of the CKM matrix element $|V_{tb}|$, one of the only free parameters in the Standard Model which has yet to be precisely measured in experiments.

The experimental observation of single top quark production only became possible in the last few years thanks to the large datasets collected by the Tevatron experiments. In 2009, the D0 [4] and CDF [5] collaborations published the first observations of the combined t- and s-channel single top quark signal in quick succession. This was followed, a few months later, by the first measurement of the t-channel cross-section by D0 [6]. The current state of single top measurements at the Tevatron is summarized in Fig. 1.1; the observed combined and t-channel cross-sections are consistent with Standard Model expectations. The cross-section for Wt-channel single top quark production is predicted to be extremely small at the Tevatron, and to date no attempt has been made to search for this process. Before the start of operations at the Large Hadron Collider, several studies of the prospects for single top cross-section measurements, including all three production modes, had been performed by both the ATLAS [7, 8] and CMS [9, 10] collaborations.

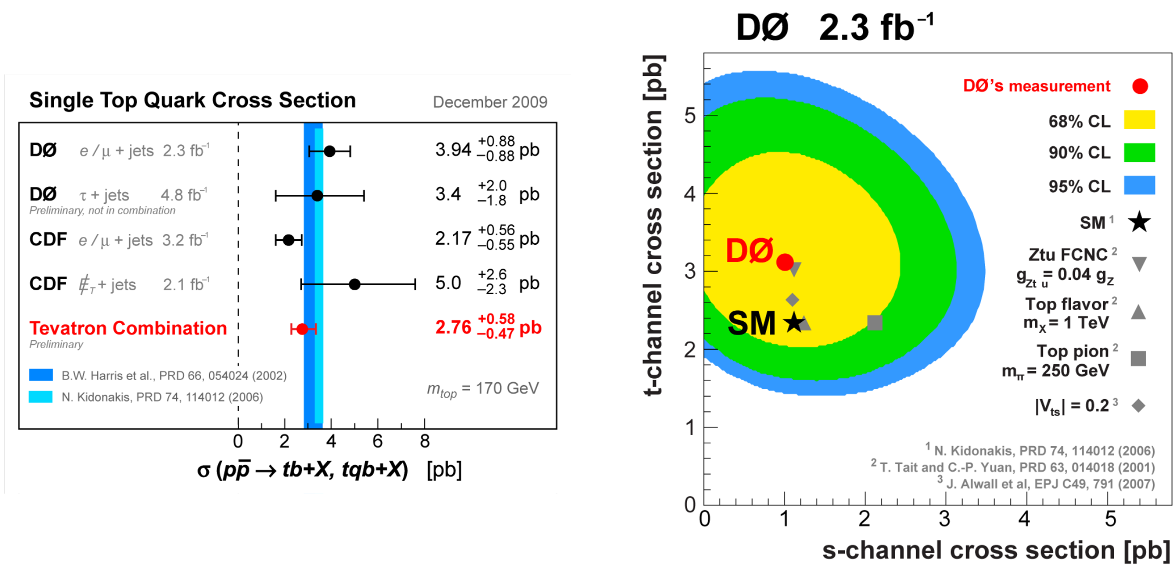

Figure 1.1: Left: Tevatron results for the combined $(t + s)$ single top quark production cross-section. Right: t-channel versus s-channel cross-section plot from D0.

This dissertation describes the first search for Wt-channel single top quark production in hadron collisions. This search is performed using 35 pb^{-1} of 7 TeV proton-proton collision data recorded between June and October 2010 with the ATLAS detector at the Large Hadron Collider. In the Standard Model, the top quark decays almost exclusively to a bottom quark and W boson, while the W boson decays either to a pair of quarks or a charged lepton and neutrino. Here, only the Wt final states where each W boson decays to either an electron or muon and the corresponding neutrino are considered. The experimental signature of these events thus consists of two oppositely-charged leptons, one high-transverse-momentum b-jet, and significant missing transverse energy due to the presence of two neutrinos.

Unfortunately, several other processes with much larger production rates also have similar signatures. Most notably, top pair production in the dilepton final states only has one additional b-jet and a production cross-section which is predicted to be approximately 11 times greater than that of the Wt signal. Z boson and WW dilepton events with a radiated jet also account for a significant fraction of the background. Finding a set of event selection criteria which yield an optimal signal purity is thus the main challenge of this analysis. This is achieved by exploiting the expected differences in the transverse momenta of the two leading jets between the signal and dominant backgrounds. Indeed, the transverse momentum of the leading jet is a very effective discriminant against the Z and WW backgrounds, while that of the subleading jet can be used to discriminate against the top pair background. These criteria are chosen to minimize the total uncertainty on the resulting cross-section measurement.

This document is organized as follows. A brief summary of the theory underlying the production and decay of top quarks is given in Chapter 2. The ATLAS detector is then described in detail in Chapter 3. The data and simulation samples used in the analysis, as well as the object selection criteria and their performance are outlined in Chapter 4. This is followed by Chapter 5, which contains the details of the event selection and background determination. Chapter 6 then describes the procedure used to evaluate the effect of uncertainties on the predicted event yields and propagate this effect to the quantity of interest, the cross-section for Wt-channel single top quark production. Finally, a summary of the results and a discussion of the future prospects for similar measurements conclude this thesis in Chapter 7.

A new and original technique for performing cross-section measurements without relying on the experimental measurement of the integrated luminosity is presented in Appendix A.

Note that natural units, where $\hbar = c = 1$, are used consistently throughout this thesis.

Chapter 2

Theoretical context

The theoretical underpinnings of single top quark production are described in this chapter. We will first review the Standard Model (SM) of particle physics, then take a closer look at the top quark's properties within the SM, and finally discuss how these properties can be modified in beyond-the-Standard-Model theories.

2.1 The Standard Model

Modern theoretical particle physics is built on the twin pillars of quantum field theory and group theory. Matter particles are represented by fermionic quantum fields which are typically charged under some gauge group, and their properties and interactions result from the allowed terms in the Lagrangian of the theory. At this time, the Standard Model [11, 12, 13, 14] constitutes the most complete theory of physics at the subatomic scale. It provides an accurate description of the properties of all known fundamental particles and their interactions through the strong, weak, and electromagnetic interactions[1]. Indeed, the existence of many particles — the $W^{\pm}$ and Z bosons, the tau neutrino, and the top quark to name a few — was predicted by the SM many years before their experimental

[1]Gravity is not included in the Standard Model, but since it is many orders of magnitude weaker than the other forces, it is almost always negligible in fundamental particle interactions.

observation became possible.

In the SM, the gauge group is $SU(3)_C \times SU(2)_L \times U(1)_Y$, where the subscript denotes the conserved charge corresponding to each subgroup: color C for $SU(3)$, weak isospin L for $SU(2)$, and weak hypercharge Y for $U(1)$. The matter fields of the SM are described in Table 2.1; there are three generations each of quarks and leptons, and each generation contains either an up-type and a down-type quark or a charged lepton and a neutrino. The SM is a chiral gauge theory, meaning that the left- and right-handed chiralities of the matter fields have different properties, as is evident from Table 2.1. In the classical Standard Model, neutrinos are assumed to be massless, so the right-handed neutrino fields are absent from the theory.

ψ	$SU(3)_C$	$SU(2)_L$	$U(1)_Y$
Q_L	3	2	1/6
U_R	3	1	2/3
D_R	3	1	-1/3
L_L	1	2	-1/2
E_R	1	1	-1

Table 2.1: Standard Model matter fields and their representations under each gauge subgroup.

The Lagrangian that describes this theory is shown in Equation 2.1, where $g_{3/2/1}$ and $G_\mu/W_\mu/B_\mu$ represent the coupling strengths and gauge fields associated with the $SU(3)$, $SU(2)$, and $U(1)$ subgroups, ψ are the fields of Table 2.1, and the indices a and b denote sums over subgroup generators and fermion generations, respectively.

$$\mathcal{L}_{SM} = -\frac{1}{4}G^a_{\mu\nu}G^{\mu\nu,a} - \frac{1}{4}W^a_{\mu\nu}W^{\mu\nu,a} - \frac{1}{4}B_{\mu\nu}B^{\mu\nu} + \sum_\psi i\bar{\psi}^b\gamma^\mu D_\mu \psi^b \tag{2.1}$$

The covariant derivative for the fermion fields is given in Equation 2.2, where λ^a (T^a) is either a Gell-Mann (Pauli) matrix, or zero if the relevant field transforms as an $SU(3)$

($SU(2)$) singlet.

$$D_\mu = \partial_\mu - ig_3\lambda^a G^a_\mu - ig_2 T^a W^a_\mu - ig_1 Y B_\mu \tag{2.2}$$

At this point, the theory is perfectly self-consistent, but is still missing some key features to become an accurate description of reality: most notably, all of the particles are massless, which clearly contradicts our experimental knowledge. Adding fermion masses m to Equation 2.1 would require adding terms of the form $m\bar{\psi}_L\psi_R$; however, such terms are not $SU(2)$ singlets and would thus explicitly break the gauge symmetry. A much more natural alternative, and as it turns out one with a number of pleasing side effects, is provided by the Higgs mechanism [15, 16, 17, 18]. First, a complex scalar doublet ϕ is introduced which transforms as an $SU(3)$ singlet, an $SU(2)$ doublet, and has hypercharge $-1/2$. It is also made to interact with the matter fields through the so-called Yukawa coupling terms, as shown in Equation 2.3, where a and b are generational indices.

$$\begin{aligned}\mathcal{L}_{Higgs} =& \left(D_\mu\phi\right)^\dagger \left(D^\mu\phi\right) - \mu^2\phi^\dagger\phi - \frac{1}{4}\lambda\left(\phi^\dagger\phi\right)^2 \\ &+ \mathcal{Y}^{ab}_U \bar{Q}^a_L \left(i\sigma_2\phi^*\right) U^b_R + \mathcal{Y}^{ab}_D \bar{Q}^a_L \phi D^b_R + \mathcal{Y}^{ab}_L \bar{L}^a_L \phi E^b_R + \text{c.c.}\end{aligned} \tag{2.3}$$

The parameter μ^2 which appears in the scalar potential is then taken to be negative, which causes the ϕ field to acquire a nonzero vacuum expectation value (VEV) proportional to $v = \sqrt{-\mu^2/\lambda}$ in one of its components. This spontaneously breaks the electroweak gauge symmetry $SU(2)_L \times U(1)_Y$ down to $U(1)_Q$, where the conserved charge of the surviving symmetry $Q = L + Y$ is the familiar electric charge. Expanding the field about its VEV and taking only the first-order term (i.e. $\phi \sim v$), then rewriting $\mathcal{L}_{Higgs}$ leads to many convenient changes in the phenomenology of the theory.

- The scalar kinetic term $\left(D_\mu\phi\right)^\dagger \left(D^\mu\phi\right)$ gives rise to a series of terms which can be combined into a mass matrix for the W_μ and B_μ gauge fields. Diagonalizing this matrix gives us the familiar $W^\pm_\mu$ and Z_μ vector bosons with their masses $M_W = vg_2/2$ and $M_Z = v\sqrt{g_1^2 + g_2^2}/2$, as well as the massless photon A_μ.

- The three components of ϕ corresponding to the broken $SU(2)$ (the Goldstone bosons) can be absorbed into a redefinition of the $W_\mu^\pm$ and Z_μ bosons; thus, they are effectively used to give the bosons corresponding to the generators of the broken symmetry the third polarization degree of freedom necessary for their having a nonzero mass.

- Rewriting the gauge part of $\mathcal{L}_{SM}$ in terms of the new gauge fields gives new three- (WWA, WWZ) and four-boson ($WWAA$, $WWAZ$, $WWZZ$) interaction terms.

- The Yukawa terms yield fermion mass matrices $\mathcal{Y}_\psi^{ab} v/\sqrt{2}$ for the up-type quarks, down-type quarks, and charged leptons. These can be diagonalized by independent $U(3)$ rotations in flavor space applied to each type and chirality of field, i.e. $\Psi_\chi = M_\chi^\psi \psi_\chi$, where $\psi = U,\ D,\ N,\ E$, $\chi = L$ or R, and M is a unitary matrix. The diagonalized mass matrices thus have the form $(M_L^\psi)^\dagger \mathcal{Y}_\psi M_R^\psi v/\sqrt{2}$. The rotations do not affect most of the theory since the fermion fields are mostly present in the combination $\bar{\psi}\psi \rightarrow \bar{\Psi}\Psi = \bar{\psi}(M^\psi)^\dagger M^\psi \psi = \bar{\psi}\psi$. The only exception is the interactions with the $W_\mu^\pm$ bosons, since these involve couplings of the up-type quarks to the down-type quarks and charged leptons to neutrinos. The relevant terms for the quarks have the form $g_2 \bar{U}_L \gamma^\mu W_\mu^+ D_L$, which in the mass eigenstate basis becomes $g_2 \bar{U}_L^a V_{CKM}^{ab} \gamma^\mu W_\mu^+ D_L^b$, where $V_{CKM} = \left(M_L^U\right)^\dagger M_L^D$ is known as the Cabbibo-Kobayashi-Maskawa (CKM) quark mixing matrix, and describes the relative strengths of the charged current couplings between each up-type and down-type quark combination.

Though the Standard Model is remarkable in its ability to reproduce all of the known features of fundamental particle interactions, it can not be called a complete theory for two main reasons. The first is that the values of several of its parameters are not determined within the theory itself. The experimentally measured values of these free parameters are listed in Table 2.2. There are 18 in total: the gauge couplings, the Higgs potential parameters μ and λ, the fermion masses/Yukawa couplings, and the CKM matrix elements, of which only four are free due to unitarity constraints. The second reason is that the Higgs mechanism, for all its benefits, also gives rise to an important dilemma known as the naturalness problem. When one attempts to calculate the loop corrections to the Higgs boson mass in the Standard Model, one finds that they depend linearly on the cutoff scale of the theory, that is, the energy scale at which the theory stops giving reliable predictions. However, the mass of the Standard Model Higgs boson is constrained by indirect experimental measurements to be smaller than 157 GeV at 95% confidence level [19]. The inevitable conclusion is that either the cutoff scale must be quite low (of order 1 TeV), meaning that Standard Model predictions should break down at the energies probed by the LHC, or the small Higgs mass must result from the almost perfect cancellation of two much larger numbers, a disturbing possibility.

2.2 The top quark

The third-generation up-type quark in the Standard Model is known as the top quark. Its weak isospin partner is known as the bottom quark. Top quarks carry an electric charge of $+\frac{2}{3}e$, where e is the positron charge, as well as one half unit of intrinsic angular momentum. Since the top quark is charged under $SU(3)$, technically, its name does not refer to a single particle, but to three fermions possessing identical properties, interactions, and quantum numbers, except for a different color charge.

The most striking property of the top quark, and indeed that which is responsible for much of its phenomenology, is its mass of $m_t = 172.0 \pm 1.6$ GeV. This value is more than 40 times that of the next heaviest Standard Model fermion. In the vocabulary of the previous section, this means that the top quark is the only particle with a Yukawa coupling of order unity, $\mathcal{Y}_t = \sqrt{2}m_t/v \sim 1$.

In hadron collisions, top quarks can either be produced as top-antitop pairs through

Parameter	Value
g_1	0.3581±0.0002
g_2	0.6531±0.0006
g_3	1.220±0.007
$v = \sqrt{-\mu^2/\lambda}$	~246 GeV
$\lvert V_{ud}\rvert$	0.97425 ± 0.00022
$\lvert V_{us}\rvert$	0.2252 ± 0.0009
$\lvert V_{ub}\rvert$	0.00389 ± 0.00044
$\lvert V_{cd}\rvert$	0.230 ± 0.011
$\lvert V_{cs}\rvert$	1.023 ± 0.036
$\lvert V_{cb}\rvert$	0.0406 ± 0.0013
$\lvert V_{td}\rvert$	0.0084 ± 0.0006
$\lvert V_{ts}\rvert$	0.0387 ± 0.0021
$\lvert V_{tb}\rvert$	0.88 ± 0.07

Particle	Mass [MeV]
u	$2.49^{+0.81}_{-0.79}$
c	$1,270^{+70}_{-90}$
t	$172,000 \pm 1,600$
d	$5.05^{+0.75}_{-0.95}$
s	101^{+29}_{-21}
b	$4,190^{+180}_{-60}$
e	$0.510998910 \pm 0.000000013$
μ	$105.6583668 \pm 0.0000038$
τ	$1,776.82 \pm 0.16$
ν_e	< 0.000002
ν_μ	< 0.19
ν_τ	< 18.2

Table 2.2: The parameters of the Standard Model [19]. The CKM matrix element values given come from experimental measurements and make no assumptions about the number of fermion generations in the SM, except for $|V_{td}|$ and $|V_{ts}|$ which assume $|V_{tb}| = 1$. The light (u,d,s) quark masses are the current masses in the $\overline{\mathsf{MS}}$ renormalization scheme, evaluated at a renormalization scale $\mu = 2$ GeV. The c and b quark masses are the running masses ($\mu = m_q$), also in the $\overline{\mathsf{MS}}$ scheme. The t quark and lepton masses given correspond to the propagator pole masses. For the massless neutrinos, the experimental 95% confidence level upper limits on the masses are given.

the strong interaction or single top quarks through the electroweak interaction. Leading-order Feynman diagrams for both production modes are shown in Figure 2.1.

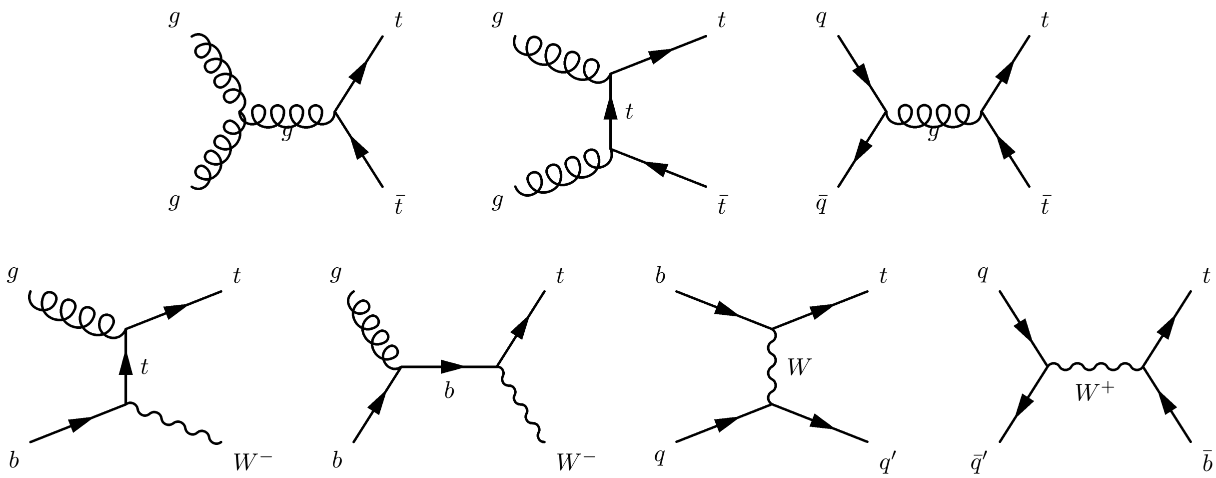

Figure 2.1: Tree-level Feynman diagrams for top pair production (top) and single top quark production (bottom) in hadron collisions. The single top diagrams depict, from left to right, the Wt-channel (2 diagrams), t-channel, and s-channel processes.

The most precise theoretical determination of the cross-section for the production of $t\bar{t}$ pairs comes from an approximate next-to-next-to-leading order (NNLO) calculation [20]. The result obtained with this approach is $\sigma_{t\bar{t}} = 165^{+11}_{-16}$ pb for $\sqrt{s} = 7$ TeV proton-proton collisions, assuming a top mass of 172.5 GeV. The dependance on the top mass of this prediction is approximated by $\Delta\sigma/\sigma \approx -5\Delta m_t/m_t$. The uncertainties shown represent an effect of around 8%, and include the effects of scale variations and parton density function (PDF) uncertainties. In pp collisions, roughly 90% of the top-antitop pairs produced are expected to originate from gg initial states, with the remaining 10% coming from the $q\bar{q}$ diagrams.

Processes resulting in the production of single top quarks usually contain a Wtb vertex, and it is useful to define three different production modes depending on the virtuality of the W boson in the interaction. If the W boson four-momentum is spacelike, the process is referred to as t-channel production or W-gluon fusion. If the W boson is on-shell, the process is called Wt-channel or associated production. Finally, the case where the W boson is timelike is known as s-channel or W^* production. The differential cross-sections for all three production modes have been calculated to next-to-leading order (NLO) in perturbation theory, and inclusive approximate NNLO results recently became available [21, 22, 23]. These are shown in Table 2.3 for a top mass of $m_t = 173$ GeV. The theoretical uncertainties at NNLO are completely dominated by the PDF uncertainties. Due to the dominance of valence u-quarks in the proton, the t- and s-channel processes are more likely to proceed from bu and $u\bar{d}$ initial states, respectively, which means that in these production modes, more top quarks are produced than antitops, as can be seen in Table 2.3.

Process	t-channel	Wt-channel	s-channel
σ_t	$41.7^{+1.8}_{-0.8}$	$7.8^{+0.5}_{-0.6}$	$3.17^{+0.14}_{-0.12}$
$\sigma_{\bar{t}}$	$22.5^{+0.9}_{-1.0}$	$7.8^{+0.5}_{-0.6}$	$1.42^{+0.06}_{-0.07}$
Total	64.2	15.6	4.59

Table 2.3: Standard Model cross-sections for the production of single top quarks in 7 TeV proton-proton collisions, in picobarns. The errors shown include the effects of scale variations as well as PDF uncertainties.

An important issue arises when considering the radiative NLO corrections to Wt-channel single top quark production. As shown in Figure 2.2, in some of the diagrams for the process $gg \to tWb$, the Wb pair originates from a second top quark. If one follows the usual modus operandi and integrates over all possible four-momenta for the intermediate top quark, the cases where $p^2 \sim m_t^2$ result in very large contributions to the cross-section. Indeed, following this approach implies that we are considering all of leading-order $t\bar{t}$ production as an NLO correction to Wt production. A number of alternative procedures have been proposed to disentangle the resonant part of the offending diagrams from the true Wt production, the simplest of which simply ignores the four-momenta values resulting in a second on-shell top quark in the calculation.

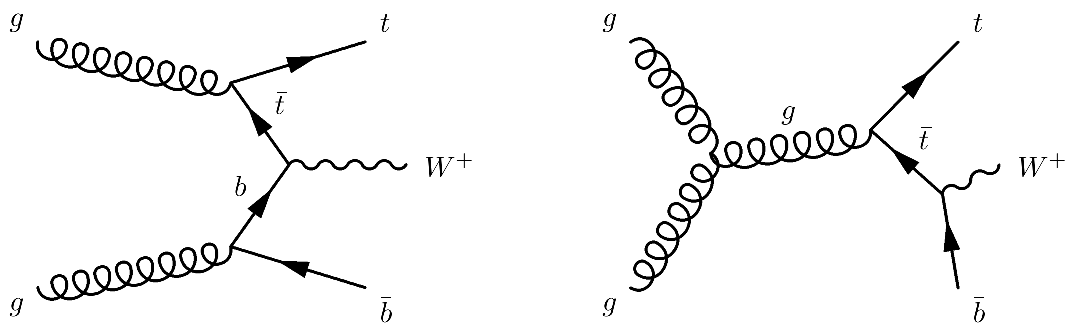

Figure 2.2: Sample Feynman diagrams contributing to the NLO Wt-channel cross-section calculation through the radiative process $gg \rightarrow tWb$. The diagram on the right must be given special treatment due to the possibility of doubly-resonant top production.

Given the large mass of the top quark and its couplings to the other SM particles, the only possible decay channels for the top quark at tree level are the weak decays to an on-shell W boson and a down-type quark, $t \rightarrow qW^+$ where $q = d$, s, or b. Assuming $M_W = m_q = 0$, the width for each of these decays is given by Equation 2.4.

$$\Gamma(t \rightarrow qW^+) = \frac{m_t^3 |V_{tq}|^2}{16\pi v^2} = |V_{tq}|^2 \times 1.76 \text{ GeV} \tag{2.4}$$

In the SM, the unitarity of the three-generation CKM matrix implies that $|V_{tb}|$ must be very close to unity, so the top decays to the down or strange quark final states are heavily suppressed. Top quarks thus decay almost exclusively to a W boson and b quark, which then undergoes hadronization. Accounting for the nonzero mass and width of the W boson, the mass of the bottom quark and adding the next-to-leading order and next-to-next-to-leading order QCD corrections and the next-to-leading order electroweak corrections changes the final quantity in Equation 2.4 to 1.28 GeV for the decay to Wb. Taking the sum of all the partial decay widths and inverting the result yields an extremely short lifetime of $\tau = 1/\Gamma = 5 \times 10^{-25}$ s. Assuming that the produced top quarks travel near the speed of light, this lifetime translates into an average decay length of around 0.15 fm. At this distance scale, the strong interaction is still in the asymptotic freedom regime, which means that in top-antitop pair production, the quarks decay before the strong force between them becomes large enough to form a hadronic bound state. The top quark is thus the only quark which does not form mesons and baryons.

The W boson is not stable and will decay almost instantly ($\tau \sim 8 \times 10^{-25}$ s) to either a charged lepton and a neutrino (32.4% of the time) or a pair of quarks which hadronize into jets (67.6% of the time). Processes such as top pair production and Wt production, in which two real W bosons are generated, can then have a wide variety of final states depending on the decay paths of the two W bosons. This has important implications for the experimental detection of these processes, and the final states are usually grouped into three categories: all-hadronic, in which both W bosons decay hadronically, lepton+jets, in which one W boson decays hadronically and the other leptonically, and dilepton, in which both W bosons decay leptonically. The lepton+jets and dilepton final states are often further subdivided depending on whether or not they contain $W \to \tau\nu_\tau$ decays, as the tau lepton's large branching ratio for decay into hadrons makes its experimental identification more challenging than electrons or muons. The relative abundance of the various final states is detailed in Table 2.4.

Decay channel	Final state particles	Branching ratio [%]
All-hadronic	$q\bar{q}' + q\bar{q}'$	45.7
e/μ+jets	$e\nu_e/\mu\nu_\mu + q\bar{q}'$	29.2
τ+jets	$\tau\nu_\tau + q\bar{q}'$	14.6
e/μ dilepton	$e\nu_e/\mu\nu_\mu + e\nu_e/\mu\nu_\mu$	4.7
τ dilepton	$e\nu_e/\mu\nu_\mu/\tau\nu_\tau + \tau\nu_\tau$	5.8

Table 2.4: Decay channels and branching ratios for events with two produced W bosons.

2.3 New physics in single top

As the previous sections have shown, the top quark possesses an extremely large mass that sets it apart from all other fundamental fermions and lies tantalizingly close to the energy scale of electroweak symmetry breaking. The Standard Model does not provide an explanation for the size of this parameter, and many [24] have speculated that it may be a sign that the top quark serves a special role in electroweak symmetry breaking. If this is the case, a natural place to look for signs of new physics phenomena would be in the electroweak interactions of top quarks, i.e. single top quark production. The ways in which 'beyond-the-Standard-Model' theories can affect single top [25] can be broadly classified into two categories depending on whether the single top rates are affected by the presence of additional fermions or bosons.

An example of a theory in which additional fermions modify the rate of production of single top quarks can be obtained by simply extending the SM to have four fermion generations instead of three. In the SM, the requirement of three-generation CKM unitarity means that $|V_{tb}|$ is already constrained to be extremely close to unity — $0.999152^{+0.000030}_{-0.000045}$ to be exact — by the measurements of the other CKM parameters. However, in a straightforward extension of the SM with a fourth generation of fermions, the charged current interactions of quarks would be governed by a 4×4 generalization of the CKM matrix, and $|V_{tb}|$ could be as small as 0.93 [26]. This would result in an identical reduction of the production cross-sections for all single top processes by a factor of $0.93^2 \sim 0.865$ relative to SM expectations.

In some theories with dynamical symmetry breaking such as the topcolor-assisted technicolor models, a scalar $t\bar{t}$ condensate can form as a result of strong dynamics at higher energies, analogous to the formation of Cooper pairs in fermionic fluids. This scalar then effectively takes over the role of the Higgs field in the SM, breaking the electroweak symmetry and generating masses for the other fermions. In these models, the large mass of the top quark and its proximity to the Higgs field VEV are thus both explained by giving the top quark a special role in bringing about electroweak symmetry breaking. These models generally predict the existence of charged, composite pseudo-Goldstone bosons named top-pions, labeled $\pi^{\pm}_{\mathrm{TC}}$, which are expected to have masses on the order of hundreds of GeV. The production and decay of these top-pions becomes a new source of s-channel single top quark production, for example through the reaction $c\bar{b} \to \pi^{+}_{\mathrm{TC}} \to t\bar{b}$, whereas the t-channel and Wt-channel production modes are predicted to be relatively unaffected.

The Standard Model of particle physics is a highly successful theory, but not without its flaws. Countless new theories have been proposed to improve upon it, many of which lead to changes in the phenomenology of single top quark production. Precision measurements of the cross-sections for all three single top quark production modes may help us determine which of these theories contains the correct description of the natural world, and as such, they are some of the most highly-anticipated results from the first few years of running at the Large Hadron Collider.

Chapter 3

Experimental apparatus

This chapter contains a detailed description of the vast experimental apparatus needed to make the research presented in this thesis possible: first, an accelerator complex which produces highly energetic and focused beams of particles and brings them into collision, and second, a multi-purpose particle detector which measures the trajectories and energies of the secondary particles resulting from those interactions.

3.1 The Large Hadron Collider

The Large Hadron Collider (LHC) [27, 28, 29] is the world's largest and highest-energy particle accelerator, located at CERN, near Geneva, Switzerland. It can function in two modes, colliding either bunches of protons or heavy ions; the research presented here only considers proton-proton collision data. The CERN accelerator complex is shown in Figure 3.1. In proton-proton mode, a beam of protons is first generated using a duoplasmatron. In this device, a cathode filament is used to fill a vacuum vessel with energetic electrons. Molecular hydrogen gas is then inserted into the vessel, where the free electrons break its atomic and molecular bonds. The resulting protons are extracted and focused into a beam using magnets. Their kinetic energy is then increased incrementally by a series of accelerators: first, to 50 MeV by a linear accelerator, then to 1.4 GeV by the circular

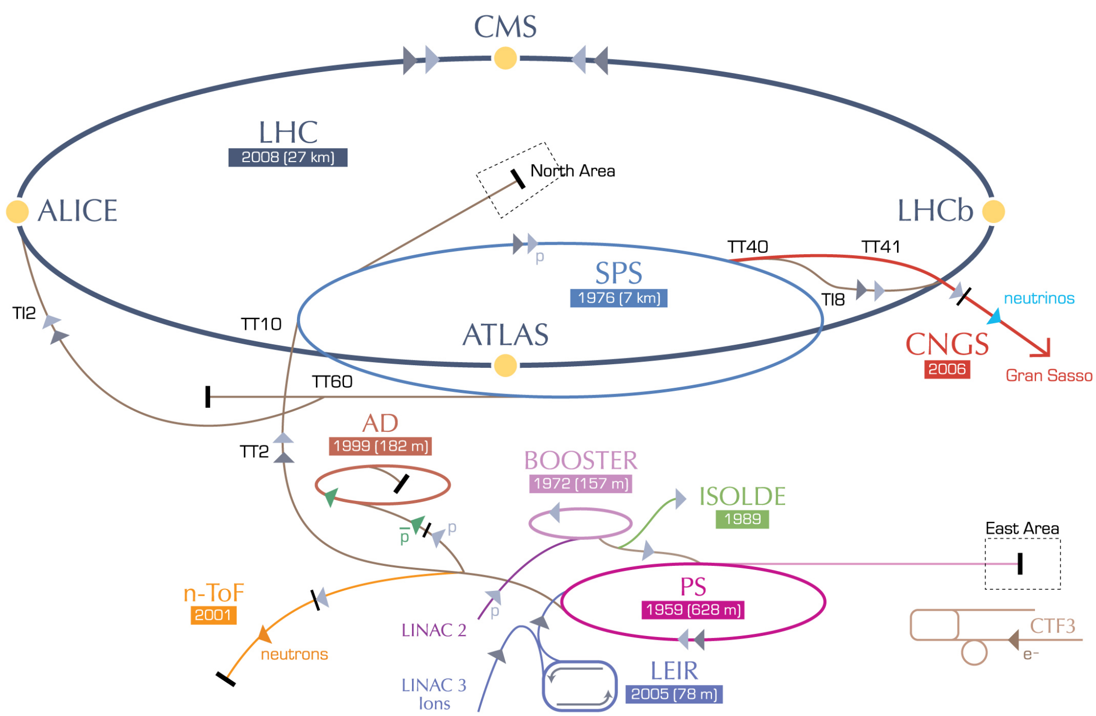

Figure 3.1: The CERN accelerator complex

Booster, then to 25 GeV by the Proton Synchrotron (PS), and finally to 450 GeV by the Super Proton Synchrotron (SPS). The 450 GeV SPS protons are then sequentially injected into the LHC's two beam pipes via separate transfer lines to become the two proton beams of the LHC. Finally, the current in the LHC's superconducting magnets is increased progressively until the target beam energy is attained and the beams are brought into collision at four interaction regions located around the ring.

The design values of the LHC's operating parameters are presented in Table 3.1 and constrasted with the optimal values attained during the 2010 running period, when the data used in this analysis were collected.

Six experiments have been built around the LHC ring to study the results of its proton-proton or heavy ion collisions. ATLAS and CMS are large, general-purpose detectors built for proton-proton physics. ALICE and LHCb are more specialized, the former for heavy ion physics and the latter for precision measurements of CP-violation in B

Parameter	Design	2010 Run
Proton energy [TeV]	7.0	3.5
Protons per bunch	1.15×10^{11}	1.1×10^{11}
Bunches per beam	2808	368
Stored energy per beam [MJ]	362	22.7
Bunch spacing [ns]	25	150
Instantaneous luminosity [$cm^{-2}\ s^{-1}$]	1.0×10^{34}	2.1×10^{32}
Mean events per bunch crossing	20	1.8

Table 3.1: Beam parameters of the Large Hadron Collider.

meson decays. Finally, LHCf and TOTEM are purpose-built experiments that study the collision products that are nearly collinear to the beamline and thus escape detection by the ATLAS and CMS detectors, respectively. The results shown here only make use of proton-proton collision data from the ATLAS detector.

3.2 The ATLAS detector

The internal structure of the ATLAS (A Toroidal LHC ApparatuS) detector [30] is shown in Figure 3.2. Like most modern general-purpose collider detectors, it employs a layered design: secondary particles flying out from the interaction point first encounter a series of tracking detectors, which measure the trajectory of charged particles, followed by calorimeters, which measure the energies of electrons, photons, and hadrons, and finally a second set of tracking detectors, which provide a second track segment and momentum measurement for minimum-ionizing muons. Neutrinos almost always escape the detector without interacting, so their presence must be inferred by looking at the energy balance in the plane transverse to the beam direction. Since the colliding particles have no momentum component in this direction, the vector sum of the momenta of the outgoing

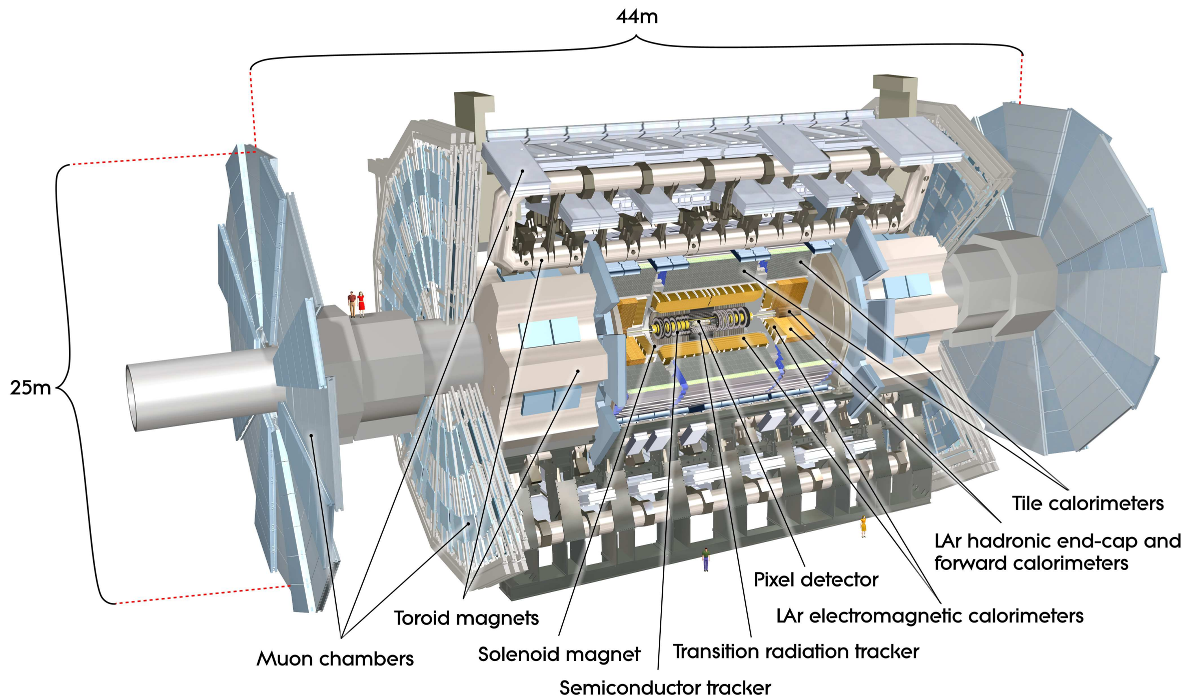

Figure 3.2: Cut-away view of the ATLAS detector

particles should be equal to the null vector. If this is not the case, the resulting missing transverse energy $E_{\mathrm{T}}^{\mathrm{miss}}$ is assumed to be attributable to the production of one or more neutrinos.

ATLAS employs a right-handed Cartesian coordinate system where the nominal interaction point is the origin, the positive x axis points toward the center of the LHC ring, the positive y axis points upwards, and the direction of the anti-clockwise proton beam defines the direction of the positive z axis. The radius r is defined as the distance from the z axis as in cylindrical coordinates, while the azimuthal and polar angles ϕ and θ are defined as in spherical coordinates. Commonly-used derived quantities are the transverse energy $E_{\mathrm{T}} = E \sin\theta$, transverse momentum $p_{\mathrm{T}} = p \sin\theta$, and pseudorapidity $\eta = -\ln(\tan(\theta/2))$. The latter quantity is used since it is approximately invariant under Lorentz boosts along the z direction, the approximation being exact in the limit of massless particles.

3.2.1 Inner detector

The region nearest to the ATLAS interaction point is equipped with three complementary tracking sub-detectors: the pixel detector, the semiconductor tracker (SCT), and the transition radiation tracker (TRT). These are immersed in an axial 2 T magnetic field provided by a 5.3 m-long solenoidal magnet. Together, they provide tracking and momentum measurements of charged particles within the pseudorapidity range $|\eta| < 2.5$.

The pixel detector and SCT are both semiconductor-based tracking detectors. Thin wafers of a semiconducting material, in this case silicon, are doped to form diodes, and electrodes are applied to the top and bottom of these wafers in a reverse-bias configuration. This forces the depletion zone to extend over the full thickness of the material. When a charged particle traverses a semiconductor, it loses energy by creating electron-hole pairs. In a semiconductor tracker, the strong electric field generated by the electrodes is used to sweep these charges away before they recombine. This motion of charge results in a current pulse which can be measured on an external circuit.

The pixel detector is comprised of three barrel sections and six endcap discs (three on each side of the detector) which together provide three space points in the pseudorapidity range $|\eta| < 2.5$. Pixel detector modules (Figure 3.3a) are 6.3 cm-by-1.9 cm-by-250 µm wafers of oxygenated silicon which are bump-bonded to 16 front-end chips on one side, while the other side provides the connections to the high voltage and cooling systems. The choice of oxygenated silicon makes the modules radiation- and inversion-hard, which allows them to survive as near as five centimeters to the interaction point. Each barrel (endcap) module can provide a position measurement with a resolution of 10 µm in the r-ϕ direction and 115 µm in the z (r) direction, which is limited by the readout pitch on the frontend chips.

The SCT is comprised of four barrel sections and 18 endcap discs (nine per side) which combine to provide four space points in the pseudorapidity range $|\eta| < 2.5$. Each SCT module is assembled from four 6.4 cm-by-6.4 cm silicon microstrip sensors with a strip pitch of 80 µm. These are combined into two layers where the top and bottom sensors are given a small stereo angle of 40 mrad. The four sensors are read out through a central front-end board which also provides the connections to the high voltage and cooling systems. Each barrel (endcap) module has a hit resolution of 17 µm in r-ϕ and 580 µm in z (r), where the former is limited by the strip pitch and the latter by the stereo angle.

The TRT is a straw tracker comprised of three barrel rings and 40 endcap wheels (20 per side) which together provide approximately 36 space points in the pseudorapidity range $|\eta| < 2.0$. It also provides electron-pion separation using transition radiation (TR): when a relativistic charged particle crosses the interface plane between two media, it loses an amount of energy proportional to its Lorentz factor $\gamma = E/m$. Due to the inverse mass dependence, for a given energy, electrons will thus emit much more transition radiation than pions or any other charged particle produced in LHC collisions. For electron energies between $1 \sim 100$ GeV, the radiation appears as nearly collinear X-ray photons. The probability of emitting a TR photon at each interface crossing is small, so incident particles must undergo a large number of transitions for a visible signal to be generated; however, the inner detector must contain only low-Z materials in order to reduce the probability that particles start showering before reaching the calorimeters. 19 µm-diameter polypropylene fibres are thus used as the radiating material, while the signal is acquired using 4 mm-diameter drift tubes filled with a $Xe/CO_2/O_2$ mixture which gives them a very high sensitivity to TR photons. They possess an intrinsic hit resolution of 130 µm in the transverse direction, which is achieved using drift time information. Due to the orientation of the drift tubes (parallel to the beam line in the barrel, radial in the endcaps), the TRT cannot provide a precision measurement of the z and r coordinates in the barrel and endcaps, respectively.

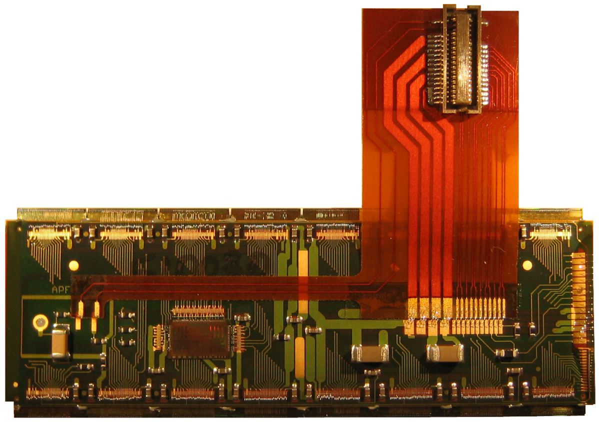

(a)

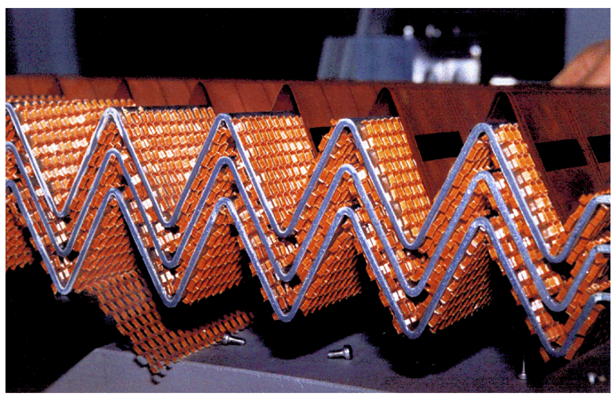

(b)

(c)

Figure 3.3: Photographs showing selected components of the ATLAS detector: pixel detector module (a), electromagnetic calorimeter section showing the accordion geometry (b), and MDT chamber structure (c).

3.2.2 Calorimetry

The ATLAS calorimeter system was designed to provide good energy resolution, fine granularity, and hermetic solid angle coverage within the region $|\eta| < 5$. Only sampling calorimeters are used: in each calorimeter subsystem, a high-radiation-length or high-interaction-length material (the absorber) is used to induce electromagnetic or hadronic showering of incident particles. The secondary particles generated in these interactions then cause the appearance of a signal when they traverse the active material. Liquid argon is used as the active material in most of the calorimeter subsystems since its response is linear with respect to particle energy and, more importantly, it is very radiation hard, meaning that no major degradation of the signal-to-noise ratio is expected over the lifetime of the experiment. However, these advantages are partially negated by the additional infrastructure needed to keep the argon in liquid form: most of the ATLAS calorimeter system has to be encased in cryostats and constantly cooled with liquid nitrogen.

In the central and endcap regions ($|\eta| < 3.2$), the electromagnetic (EM) calorimeters use lead plates as the absorber and liquid argon as the active material, arranged in an accordion design (see Figure 3.3b) to provide hermetic ϕ coverage. The thickness of the lead plates varies between 1.1 and 2.2 mm, while that of the liquid argon gaps is a constant 4.0 mm in the barrel section and varies between 0.9 and 3.0 mm in the endcap. The overall depth of the calorimeter varies between 22 and 38 radiation lengths depending on the angle of incidence. The signal deposited into the liquid argon is read out using electrode plates which bisect the liquid argon gaps. The voltage applied to these electrodes is varied to maintain a constant 450 ns drift time throughout the subdetector. The granularity of the readout in the innermost layer of the calorimeter was made particularly fine in order to allow for the effective separation of single photons from $\pi^0 \to \gamma\gamma$ decays; overall, the size of the calorimeter cells (the finest readout units) never exceeds $\Delta\eta \times \Delta\phi = 0.1 \times 0.1$. A presampler consisting of a series of 2 mm thick liquid argon layers set just inside the cryostat cold wall is used to correct for energy loss upstream of the calorimeter in the region $|\eta| < 1.8$.

Hadronic calorimetry in the central region ($|\eta| < 1.7$) is provided by a scintillating tile calorimeter which uses 14 mm-thick steel plates as the absorbing material. The radial depth of the calorimeter is approximately 7.4 interaction lengths. Signal acquisition is done using 3 mm-thick polystyrene tiles: scintillation photons from these tiles cause the emission of wavelength-shifted photons in fibers lining the sides of the tiles; these secondary photons are then detected by photomultiplier tubes located along the outer edge of the calorimeter. The 64 azimuthal wedges of the calorimeter are separated by readout gaps totalling approximately 2.6 degrees. Fibers are combined at the photomultipliers to subdivide the calorimeter into cells whose sizes range between $\Delta\eta \times \Delta\phi \sim 0.1 \times 0.1$ and 0.2×0.1.

The hadronic endcap calorimeters (HEC) use large 25 or 50 mm-thick circular copper plates separated by 8.5 mm liquid argon gaps, and cover the pseudorapidity region $1.5 < |\eta| < 3.2$. The average amount of material encountered by an incident particle which goes through the full subdetector is approximately 10 interaction lengths. Signal readout is accomplished using three electrode sheets which subdivide each liquid argon gap. A potential difference of 1.8 kV is applied to these electrodes, resulting in a signal drift time of approximately 430 ns. Etchings on the electrode sheets are used to subdivide the calorimeter into projective cells, the size of which varies between $\Delta\eta \times \Delta\phi \sim 0.1 \times 0.1$ and 0.2×0.2.

Finally, in the forward regions ($3.1 < |\eta| < 4.9$), electromagnetic and hadronic calorimetry are provided by the two Forward Calorimeters (FCal). These are separated longitudinally into three 45 cm-deep compartments, which share a similar design in order to cope with the high particle fluxes present at high $|\eta|$. Instead of electrode plates as in the other liquid argon calorimeters, the FCals employ tubular electrodes which traverse the calorimeter in the axial direction. Small ($0.25 \sim 0.50$ mm) liquid argon gaps are used in order to avoid ion buildup and ensure a small drift time while maximizing the density of the calorimeter. Copper plates were chosen as the absorber for the first compartment due to their high thermal conductivity, while the second and third compartments use tungsten slugs to ensure full shower containment and minimize lateral shower spread. The full depth of the calorimeter at normal incidence represents 208 radiation lengths and 10 interactions lengths of material, of which 28 radiation lengths and 2.7 interaction lengths are due to the first compartment.

3.2.3 Muon spectrometer

The four subsystems which comprise the muon spectrometer use a wide variety of gas-based detector designs to provide triggering capabilities and high-precision tracking for muons with $p_T > 3$ GeV and $|\eta| < 2.7$. Superconducting magnets are used to curve the muon trajectories as they exit the hadronic calorimeters, which also allows the muon spectrometer to provide a second momentum measurement for these particles. The magnet system required to do this is very extensive: the barrel toroid system contains eight 5 m-by-25 m air-core toroidal magnets, while the two endcap toroids each contain eight additional 3.5 m-by-3.5 m magnets employing a similar design. At nominal current, the azimuthal magnetic field generated has a strength of approximately 0.5 T in the barrel region and 1.0 T in the endcaps.

Monitored drift tube (MDT) chambers provide high-precision tracking over most of the muon spectrometer acceptance ($|\eta| < 2.7$). These are arrays of 3 cm-diameter aluminium tubes filled with an Ar/CO_2 mixture and fitted with a central W/Re sense wire. Each chamber (see Figure 3.3c) contains two sets of three to four layers of tubes separated by a rigid aluminium frame which houses an optical alignment system used to monitor the frame for mechanical deformations. Since the toroid magnetic field bends the particle trajectories in the polar direction, the tubes are oriented azimuthally in both the three sets of barrel chambers and eight endcap wheels. Each tube possesses an excellent hit resolution of 80 µm in the z (r) direction in the barrel (endcap) chambers, but no measurement of the transverse coordinate is possible, so the precision ϕ measurement must be provided by the trigger chambers. The choice of individual tubes for the MDT makes it a very robust system, as the failure of a single tube does not affect the others; however, the long (up to 0.7 µs) pulse trains caused by ionization far from the sense wire severely limit their rate capability.

In the low-r regions of the innermost endcap wheels ($2 < |\eta| < 2.7$), particle fluxes are much higher, so precision tracking is accomplished using cathode strip chambers (CSC). These are also gas-based detectors; however, as opposed to the TRT and MDT, they are wire chambers, so they use a common gas volume containing a plane of sense wires surrounded by two cathode plates. In the case of the CSC, the upper and lower cathode plates have also been segmented into strips in perpendicular directions, thus allowing for the simultaneous measurement of two coordinates. The distance between adjacent wires and the anode-cathode spacing are both 2.54 mm. The strip pitch in the r (ϕ) direction varies between $3 \sim 5.6$ mm ($12.5 \sim 21$ mm), resulting in a hit resolution of 40 µm (5 mm). Each chamber contains four gas volumes, and can thus provide four position measurements.

As Section 3.2.5 will reveal, the Level-1 trigger decision must be taken within 2.5 µs of each bunch crossing. Coupled with the LHC's 40 MHz collision rate, this means that the muon trigger chambers must be capable of handling extremely high hit rates and generate very narrow signal pulses. Resistive plate chambers (RPC) operated in avalanche mode handily satisfy both of these requirements and are used to trigger on muons in the barrel region ($|\eta| < 1.15$). The active medium in the RPC is a 2 mm-thick gas gap which is sandwiched by two plastic laminate plates, then by two electrode plates, and finally by two sets of orthogonal metallic pickup strips. The electric field and gaseous mixture in the gap are tuned so that when a charged particle ionizes the gas, it initiates electron avalanches which are read out by the pickup strips through capacitive coupling. The detector elements are thus completely wireless, which makes for a very robust design. Three sets of RPC are mounted on the middle and outer barrel MDT chambers, and each RPC contains two gas gaps, so up to six independent position measurements can be provided. The pitch of the readout strips is identical in the z and ϕ directions and varies between 23-25 mm, resulting in a single-hit position resolution of 10 mm on both of these coordinates.

Thin gap chambers (TGC), another variety of wire chamber, are used to trigger on muons in the endcap regions ($1.05 < |\eta| < 2.4$). As the name suggests, in the TGC, the anode-cathode spacing (1.4 mm) is made smaller than the wire pitch (1.8 mm) in order to reduce the signal collection time, thus improving the time resolution of the detector. The anode wires are strung along the azimuthal direction, and the readout of the electron signal provides a measurement of the bending coordinate (r) with a resolution of $2 \sim 6$ mm. The cathode plates are made of FR4 coated with a thin layer of graphite on the inner surface, while the outer surface has a copper cladding which is kept at ground. In some chambers, the copper sheet is segmented into radial strips which are connected to amplifiers to provide a measurement of the ϕ coordinate with a resolution of $3 \sim 7$ mm.

3.2.4 Other sub-detectors

The ATLAS detector also contains several smaller (in terms of number of readout channels) sub-detectors which nevertheless perform a variety of vital tasks. These are briefly described in this section.

The ATLAS Beam Conditions Monitor (BCM) system consists of two sets of four modules located within the inner detector volume at $z = \pm 184$ cm. Each module contains a pair of synthetic diamond sensors read out in parallel using fast electronics. The use of diamond makes the sensors extremely radiation hard, which allows them to be positioned only 5.5 cm from the beamline, corresponding to a pseudorapidity of approximately 4.2. The main role of the BCM is to monitor beam background levels using its sub-nanosecond hit timing resolution: when secondary particles from upstream interactions go through ATLAS, they will cause "early" hits in the near BCM station at a time $t = -z$ relative to the nominal collision time, while secondary particles from normal collisions reach both sets of BCM modules at time $t = +z$. These "in-time" hits can also be used to provide a high-purity trigger for minimum bias events or monitor the instantaneous luminosity of individual bunches in the LHC beams, which makes the BCM a very versatile detector despite its simple design.

LUCID (Luminosity measurement using Cerenkov Integrating Detector) is the main subdetector used for relative luminosity monitoring in ATLAS. It consists of two arrays of twenty aluminium tubes located at $z = \pm 17$ m and $r \sim 10$ cm, which translates to $|\eta| \sim 5.8$. Each tube is filled with C_4F_{10} and the end facing away from the interaction point is read out with a photomultiplier tube (PMT). When a secondary charged particle with sufficient energy enters the gas volume, it emits Cerenkov radiation with a half-angle of 3° which is detected by the PMT. One important feature of Cerenkov radiation is that its spectrum does not have a Landau tail, which means that the signal seen by the PMTs can be used to infer the number of incident secondary particles. By counting the number of particles in LUCID and normalizing to the average expected in single inelastic proton-proton collisions, one can thus monitor the bunch-by-bunch instantaneous luminosity and measure the overall integrated luminosity delivered to ATLAS.

3.2.5 Trigger and data acquisition

The main role of the ATLAS trigger and data acquisition (TDAQ) system is to bridge the gap between the LHC collision rate of 40 MHz and the rate at which events can be written to disk, approximately 200 Hz. This is accomplished in three steps, which are known as Level 1, Level 2, and Event Filter; the last two are sometimes collectively referred to as the High Level Trigger (HLT) since they share the same infrastructure.

At Level 1 (L1), the event rate is reduced to 75 kHz using limited information from the muon spectrometer and calorimeters. In the former, custom electronics are used to perform rudimentary tracking for six muon p_T thresholds using the η coordinate hit information from the trigger chambers (RPC and TGC), while in the calorimeters, specialized front-end boards are used to sum the calorimeter energy within reduced-granularity, projective "trigger towers", perform clustering, and compute the missing and total transverse energy of the event. This information is condensed into 150 digital signals which are sent to the Central Trigger Processor (CTP), where they are formed into trigger conditions using lookup tables. The trigger conditions are then combined into as many as 256 trigger items following the trigger menu. Prescaling is used to limit the trigger rates of individual items — this refers to the practice of only recording one event for every N that satisfy the trigger conditions. The corresponding item is then said to have a prescale of N, or to be unprescaled if $N = 1$. An event is accepted if it passes any of the 256 trigger items after the application of prescaling.

During the L1 latency of up to 2.5 μs, the data is temporarily stored in buffers on the front-end electronics of each subdetector. When an event passes the L1 trigger, an accept signal is sent by the CTP to the subdetector readout drivers (ROD), which pull the data off the front-ends, format it, and send it to the readout system, where it is temporarily stored on readout buffers. The CTP decision for each trigger item is also sent to the Region of Interest (RoI) builder, which uses this data to identify the regions of the detector containing physics objects that fired the L1 triggers.

The types of objects and their locations are forwarded to the Level 2 (L2) trigger system, which requests the complete detector information within the RoI, corresponding to 1-2% of the total data volume, from the readout system and assigns it to a node on the L2 cluster. Tracks are built from the inner detector hits, allowing for the first time a separation between electrons and photons. The event rate is reduced to 3.5 kHz, and the L2 decision is typically available after around 40 ms.

If the event is accepted at L2, the detector data is transferred from the readout buffers to a node on the event building cluster, where full reconstruction of the event is performed including tracking, b-tagging, jet finding, and identification of electrons, photons, and hadronic tau lepton decays. The result is then sent to a node on the event filter (EF) cluster, where the last step in the trigger selection occurs. Depending on which triggers are passed at the EF stage, the event is also classified into different data streams.

An important property of any triggering system is the amount of dead-time, that is, time during which the trigger is not actively accepting or rejecting events, introduced into the readout chain. In ATLAS, the only source of dead-time is the CTP: in order to avoid overlapping readout windows in the subdetectors with slower charge collection, the CTP is inactive for five bunch crossings following every L1 accept, resulting in a minimum dead-time fraction of 0.9%. A leaky bucket algorithm implemented in the CTP hardware introduces additional dead-time when the rate of L1 accepts exceeds 7 per 2905 bunch crossings; this is done to ensure that the front-end buffers do not overflow.

3.2.6 Performance

The performance of the ATLAS sub-detector systems during the 2010 run is summarized in Table 3.2. Of the 48.1 pb^{-1} of integrated luminosity delivered by the LHC during stable beam periods, 45.0 pb^{-1} were recorded by ATLAS, resulting in a data-taking efficiency of 93.6%. The losses are attributable either to deadtime in the TDAQ system/problems with individual sub-detectors which prevented ATLAS from going into data-taking mode (4.4%), or to the short period of time needed after stable beams are established to bring the tracking detectors up to nominal voltage (2.0%). All of the design goals of the detector have thus been met or surpassed, and its operational performance during the data-taking period used in this analysis was close to optimal.

Sub-detector	Number of channels	Operational fraction [%]	Good data fraction [%]
Pixel	80M	97.2	99.1
SCT	6.3M	99.2	99.9
TRT	350k	97.5	100
EM calo	170k	99.9	90.7
Tile calo	9,800	98.8	100
HEC	5,600	99.8	96.6
FCal	3,500	99.9	97.8
MDT	350k	99.8	99.9
CSC	31k	98.5	96.2
RPC	370k	97.0	99.8
TGC	320k	99.1	99.8

Table 3.2: Performance of the ATLAS sub-detectors during the 2010 run. The good data fraction is computed using only stable beam periods with the tracking detectors turned on and the TDAQ system functioning normally.

Chapter 4

Samples and physics object selection

This chapter contains a detailed description of the data and simulation samples used in this thesis, as well as the procedure used to reconstruct and identify final state physics objects of interest: jets, electrons, muons, and missing transverse energy.

4.1 Data sample

Data-taking at ATLAS is divided into continuous time periods referred to as runs. The data used in this analysis were obtained by running the Large Hadron Collider in proton-proton mode at a center-of-mass energy of 7 TeV between June and October 2010. Runs collected between March and May 2010, corresponding to an integrated luminosity of approximately 0.85 pb^{-1}, are discarded because the HLT was not active or the performance of the single lepton triggers was sub-optimal. After the end of a run, the recorded data is reconstructed and hundreds of histograms of basic quantities are produced and compared with the expected distributions. This is referred to as data quality monitoring, and is used to search for abnormalities in the detector performance. Here, only runs for which all detector and trigger subsystems pass the data quality tests are used. This requirement reduces the amount of data available for analysis from 45 pb^{-1} to 35 pb^{-1}.

4.2 Monte Carlo simulation samples

In experimental high-energy physics, hypotheses are often tested by comparing experimental data with the results of Monte Carlo simulations of the various physical processes of interest. These simulations are produced in three sequential stages:

1. Generation, in which a random occurence of a given physical process is created, including the decays of unstable particles. Free partons (quarks or gluons) resulting from the interaction are converted to jets of hadrons by first applying a parton shower model, which simulates the energy loss of the parton by emission of (mostly) collinear quarks and gluons, then a hadronization model, which joins the resulting mass of quarks and gluons into color-neutral hadrons such as pions and kaons.

2. Simulation, in which the collision products propagate outward through the detector, losing energy in the detector material.

3. Digitization, in which the energy deposits are converted to electrical signals by using software models for the conversion of the deposited energy to free charges, the propagation of these charges in the active medium of the detector, and the effect of the front-end electronics.

The output of digitization is a record of the "observed" detector signals, for all intents and purposes identical to that obtained from real collisions.

As shown in Table 4.1, different software tools are used to perform the first step of the event generation for the signal and background processes relevant to this analysis. Wt signal events are generated using the full differential NLO calculations implemented in MC@NLO version 3.41 [31]. The NLO cross-section predicted by MC@NLO assuming a top quark mass of 172.5 GeV is also used to normalize the expected signal yields. The overlap of the Wt process with top quark pair production at next-to-leading order, as first introduced in Section 2.2, is resolved using the diagram removal scheme [32], in which the problematic NLO diagrams are simply removed from the Wt cross-section calculation.

Process	Generator	Filter requirements	$\sigma \times BR$ [pb]
Wt	MC@NLO	—	14.6
$t\bar{t} \to b\ell\nu + X$	MC@NLO	—	89.7
$Z \to \ell\ell+$ 0 parton	ALPGEN	$10 < M_{\ell\ell} < 40$ GeV	3,819.0
$Z \to \ell\ell+$ 0 parton	ALPGEN	$40 < M_{\ell\ell} < 2,000$ GeV	835.4
$Z \to \ell\ell+$ 1 parton	ALPGEN	$10 < M_{\ell\ell} < 40$ GeV	106.1
$Z \to \ell\ell+$ 1 parton	ALPGEN	$40 < M_{\ell\ell} < 2,000$ GeV	168.0
$Z \to \ell\ell+$ 2 partons	ALPGEN	$10 < M_{\ell\ell} < 40$ GeV	51.8
$Z \to \ell\ell+$ 2 partons	ALPGEN	$40 < M_{\ell\ell} < 2,000$ GeV	50.6
$Z \to \ell\ell+$ 3 partons	ALPGEN	$10 < M_{\ell\ell} < 40$ GeV	10.5
$Z \to \ell\ell+$ 3 partons	ALPGEN	$40 < M_{\ell\ell} < 2,000$ GeV	14.0
$Z \to \ell\ell+$ 4 partons	ALPGEN	$10 < M_{\ell\ell} < 40$ GeV	2.4
$Z \to \ell\ell+$ 4 partons	ALPGEN	$40 < M_{\ell\ell} < 2,000$ GeV	3.6
$Z \to \ell\ell+$ 5 partons	ALPGEN	$10 < M_{\ell\ell} < 40$ GeV	0.6
$Z \to \ell\ell+$ 5 partons	ALPGEN	$40 < M_{\ell\ell} < 2,000$ GeV	1.0
WW	HERWIG	1 lepton with $p_{\mathrm{T}} > 10$ GeV, $\|\eta\| < 2.8$	17.0
WZ	HERWIG	1 lepton with $p_{\mathrm{T}} > 10$ GeV, $\|\eta\| < 2.8$	5.5
ZZ	HERWIG	1 lepton with $p_{\mathrm{T}} > 10$ GeV, $\|\eta\| < 2.8$	1.3

Table 4.1: Monte Carlo simulation samples used in the analysis.

Top quark pair production constitutes the dominant background to this analysis due to the very similar topology of its dilepton final states, which are distinguished from signal events only by the presence of an additional b-jet. The background from top quark pairs is also obtained from MC@NLO, and is normalized to the approximate NNLO cross-section result assuming a top quark mass of 172.5 GeV as obtained from the HATHOR [20] cross-section calculator. Z/γ^* boson events with associated partons, henceforth simply referred to as Z+jets, also constitute an important background in the dielectron and dimuon decay modes due to the comparatively large production rate of Z bosons. These are generated for two invariant mass ranges using the leading-order generator ALPGEN, version 2.13 [33], which properly implements all Z/γ^* interference effects. The ALPGEN cross-sections are rescaled by a factor of 1.25 to normalize the sum of the 0/1/.../5-jet contributions to the inclusive NNLO cross-section result obtained from FEWZ [34], a software package which implements full NNLO calculations of inclusive vector boson cross-sections, in the invariant mass range $40 < M_{\ell\ell} < 2000$ GeV. Finally, despite their relatively small production rate, events containing vector bosons pairs, henceforth referred to as diboson events, are also a significant background as they naturally generate signatures containing multiple leptons and missing transverse energy. For these events, we use the leading-order generator HERWIG [35] and normalize to the next-to-leading order cross-sections as obtained from MCFM 5.8 [36]. The theoretical cross-section calculations and the generation of events use the CTEQ66 [37], CTEQ6L1 [38], and MRST2007LO* [39] parton distribution function sets for the MC@NLO, ALPGEN, and HERWIG generators, respectively. The parton showering and hadronization for all processes are done in HERWIG, with the JIMMY [40] package handling multi-parton interactions. Underlying event activity is modeled using a custom HERWIG tune based mostly on ATLAS observations at $\sqrt{s} = 900$ GeV and 7 TeV [41].

The output particles from the generation step are then propagated through a full simulation of the ATLAS detector [42] based on the GEANT4 toolkit [43]. The digitization of the resulting signals is done using subdetector-specific software packages.

Since the LHC collides bunches of protons rather than single protons, there is always the possibility of multiple inelastic proton-proton interactions occuring within the same bunch crossing. Indeed, a large fraction of the recorded data sample used in this analysis was taken at high instantaneous luminosities, where this phenomenon, which will be referred to as pileup, is far from negligible. The effect of these additional interactions is taken into account in the simulations by adding the energy deposits resulting from a random number of non-diffractive inelastic collisions derived from a Poisson distribution with a mean of 2.2 to the event of interest before the digitization stage. Some sub-detectors are also sensitive to late signals coming from the interactions of neighboring bunches; this is addressed by also adding time-shifted energy deposits to simulate the effect of up to six successive bunch crossings. This configuration corresponds to the expected conditions during the running period accounting for most of the recorded data sample. However, the remaining data were obtained under different beam configurations, so the simulation samples do not represent a faithful description of the full data sample. We therefore reweight selected simulation events depending on the observed number of good primary vertices to reproduce the distribution seen in data. The effect of this procedure on a purified sample of Z boson events is shown in Figure 4.1.

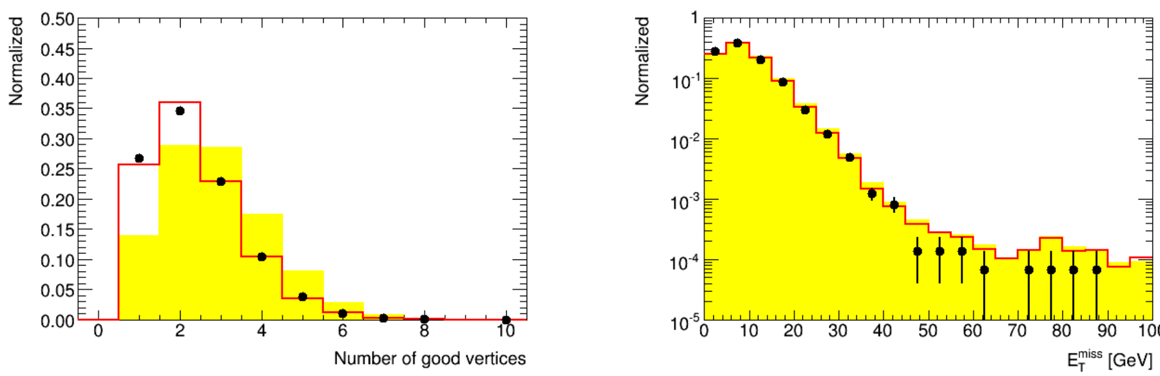

Figure 4.1: Normalized distributions for the number of good primary vertices (left) and missing transverse energy (right) seen in the full data sample (black markers) and simulation before (yellow histogram) and after (red line) applying the pileup reweighting procedure.

4.3 Trigger requirements

The data sample used in this analysis is obtained by requiring that events pass a series of single electron or muon trigger requirements. The digitization stage discussed in Section 4.2 includes a full simulation of all three levels of the trigger system, so trigger requirements are also applied on the Monte Carlo samples. The main factors motivating the choice of specific triggers are the lepton $E_{\mathrm{T}}/p_{\mathrm{T}}$ requirements and the prescale values: in order to ensure that every interesting data event is selected and to maximize signal acceptance, we always use the unprescaled trigger chain with the lowest threshold.

The e15_medium trigger chain was used to select events containing electron candidates for the full period of data-taking. It is also used to select simulation events containing electrons. This chain first requires the presence of a cluster of four electromagnetic calorimeter trigger towers with more than approximately 10 GeV of transverse energy at L1. At L2, tracking information from the inner detector is added and a rough matching in η and ϕ is demanded between the track and cluster found in each RoI. Finally, at the event filter level, the full detector information becomes available, so more stringent requirements are applied on the calorimeter shower shape and inner detector track quality.

Due to the rapid rise of the instantaneous luminosity during 2010 data-taking and the consequent changes in the ATLAS trigger configuration, three different trigger chains were used to select events containing muon candidates: mu10_MSonly, mu13, and mu13_tight. The mu10_MSonly chain requires the presence of aligned hits in the muon trigger chambers at L1, matched to a muon spectrometer track segment with p_{T} greater than 7-8 (8-9) GeV at L2 (EF). The mu13 chain has the same requirement at L1, but uses the inner detector information in the two HLT stages, requiring the presence of a combined muon track with p_{T} greater than 13 GeV at L2 and EF. Finally, the mu13_tight chain uses the same HLT algorithms as mu13, but preceeds them with a stronger L1 constraint which requires that the hit pattern in the muon trigger chambers be consistent with a muon having $p_{\mathrm{T}} > 10$ GeV.

4.4 Object reconstruction and selection

4.4.1 Electrons

The typical signature of electrons in the ATLAS detector contains one charged particle track in the inner detector pointing to a narrow energy deposition in the electromagnetic calorimeters. The electron candidates for this analysis are reconstructed using a cluster-based procedure. Electromagnetic calorimeter cells are first combined into projective 'towers' and the cell energies within each tower are summed. Energetic pre-clusters are then formed using a sliding window algorithm: a window of size $\Delta\eta \times \Delta\phi \sim 0.075 \times 0.125$ moves around the $\eta - \phi$ grid of towers, and at each point, the transverse energies of the towers within the window are added and compared with a threshold of 2.5 GeV to obtain the position of all pre-clusters. Overlaps are resolved by dropping the lower E_{T} member of each pair of pre-clusters satisfying $|\Delta\eta| < 0.05$ and $|\Delta\phi| < 0.05$.

The next step is to search for inner detector tracks pointing to each pre-cluster. We first select tracks having $p_{\mathrm{T}} > 0.5$ GeV whose η and ϕ coordinates relative to the origin are within 0.05 and 0.10 units of the pre-cluster position, respectively. The preselected tracks are then extrapolated to the second layer of the calorimeter and ordered in increasing ΔR, where the distance is computed using the weighted pre-cluster position in the second layer. The track with the lowest ΔR value is taken as the best match, and is combined with the pre-cluster to form an electron candidate. The final cluster is obtained by extending the pre-cluster size to $\Delta\eta \times \Delta\phi \sim 0.075 \times 0.175$ in the barrel section and 0.125×0.125 in the endcap.

We require that the E_{T} of the electron, as computed using the total cluster energy and track pseudorapidity, be greater than 20 GeV to ensure a uniform trigger efficiency for all selected electrons. The calorimeter cluster is required to satisfy $|\eta| < 2.47$ in order to fall within the combined fiducial region of the inner detector and electromagnetic calorimeter; however, candidates satisfying $1.37 < |\eta| < 1.52$ are vetoed, as this pseudorapidity region corresponds to the transition between the barrel and endcap electromagnetic calorimeters, and is thus poorly instrumented. A run-dependent object quality map is also applied to reject electrons in regions of the calorimeter with known hardware problems. This results in a loss of acceptance of less than 1% for signal electrons.

At this stage, most selected electron candidates actually come from particle jets, converted photons, and other sources of non-isolated or 'fake' electrons. We thus demand that candidates pass a set of electron quality cuts that includes stringent requirements on the amount of energy leakage in the hadronic calorimeter, the shape of the energy shower in the first and second layers of the electromagnetic calorimeter, the quality of the inner detector track, the matching between the track and cluster both in terms of position and energy/momentum, and the transition radiation information provided by the TRT.

However, even after the application of these criteria, fake electrons still form a significant fraction of the electron candidate sample. In single top events, the electrons of interest come from the decays of prompt W bosons and are expected to be isolated, meaning that we do not expect any nearby energy deposits or tracks. We therefore require that the sum of the calorimeter cell energies and track momenta in an $\eta - \phi$ cone with radius 0.3 around the candidate direction be less than 15% and 10% of the electron's E_{T}, respectively, after removing the contributions from the electron itself. These variables are plotted in Figure 4.2, showing that the selected cut values achieve excellent discrimination against fake electrons while keeping the acceptance for real electrons high in signal events.

4.4.2 Jets

Any quarks and gluons produced in the primary interaction or as initial or final state radiation will evolve into collimated jets of hadronic particles. These jets appear in the ATLAS detector as localized energy deposits in the electromagnetic and hadronic

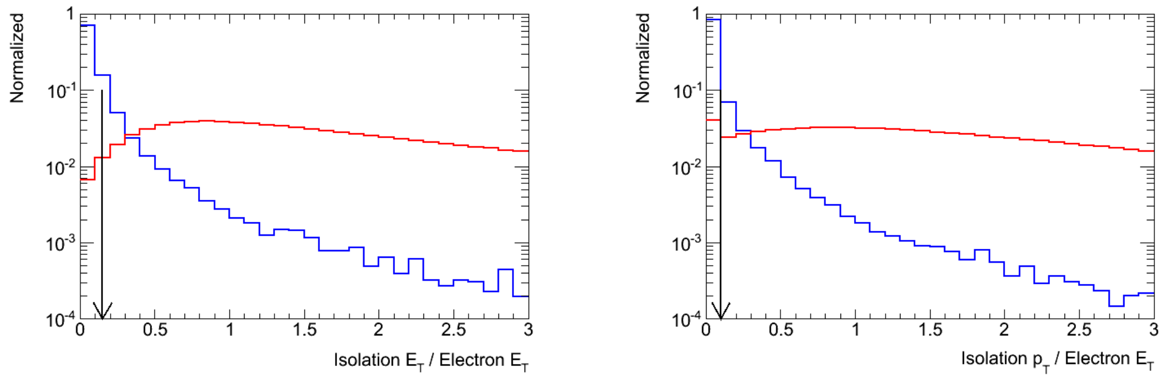

Figure 4.2: Normalized distributions for the calorimeter (left) and tracker (right) isolation variables used in electron identification. The blue and red curves are due to prompt and fake electrons in simulated signal events, respectively.

calorimeters. If the jet falls within the acceptance of the inner detector ($|\eta| < 2.5$), charged particle tracks may also be found, but these are not used.

The reconstruction of particle jets starts with the identification of calorimeter energy clusters. Calorimeter cells, including both the electromagnetic and hadronic systems, are combined using a three-dimensional topological clustering algorithm whose goal is to reduce the effect of calorimeter noise. First, all cells having energy content greater than $4\sigma_{\text{noise}}$, where σ_{noise} is the standard deviation of the cell noise distribution as measured in dedicated runs, are marked as seeds. A cluster is then formed around each seed by iteratively adding neighboring cells if their energy content is greater than $2\sigma_{\text{noise}}$. In the final step, the cells bounding each cluster are added to it regardless of their energy content.

The topological clusters are combined to form particle jets using the anti-k_t algorithm [44]. The quantities $d_i = \frac{1}{p_{\mathrm{T},i}^2}$ and $d_{ij} = \min(\frac{1}{p_{\mathrm{T},i}^2}, \frac{1}{p_{\mathrm{T},j}^2})\frac{\Delta R}{D}$ are first computed for each cluster i and each cluster pair ij, where ΔR is the distance in $\eta - \phi$ space between the two clusters and D is a distance parameter. The minimum of this set of numbers is then identified; if it comes from a d_{ij}, the corresponding clusters are merged, whereas if it comes from a d_i, the corresponding cluster is removed from the list of clusters and promoted to a jet. These two steps are repeated until all clusters have been combined into jets. The net effect of this algorithm is to sequentially combine energy depositions around the highest-p_T clusters while ensuring that the distance between the resulting jets is always at least of order D. This procedure has a number of advantages when compared with cone algorithms or other recombination algorithms. In particular, since the priority is given to high-p_T clusters, the algorithm is insensitive to collinear splitting, emission of soft partons, and pileup. In this analysis, a distance parameter of $D = 0.4$ is used, as the particle jets in the events of interest come from the decays of heavy objects (t,W) and are thus expected to be well collimated.

Due to the non-compensating nature of the ATLAS calorimeters and energy lost in material before the calorimeters, the total energy contained in each jet is less than that of its parent parton. An offline jet energy scaling procedure must thus be applied to each jet in order to obtain an estimate of the original parton energy. The component of the measured jet energy coming from pileup is first subtracted out, and the jet position is corrected to point to the primary vertex position rather than the center of the detector. An E_T- and η-dependent scale factor is then introduced which, when applied to the measured jet energies in Monte Carlo simulations, on average correctly reproduces the energies of the primary partons as contained in the truth record of the events.

Only jets having calibrated $E_T > 20$ GeV and $|\eta| < 4.5$ are used in this analysis. Since electrons are also characterized by energy deposits in the calorimeters, they almost always survive the jet reconstruction procedure. In order to avoid double-counting these objects, we thus reject the jet nearest to every selected electron candidate if the distance in $\eta - \phi$ between the two objects is less than 0.2.

4.4.3 Muons

Minimum-ionizing muons leave a distinctive signature in the ATLAS detector consisting of a charged particle track in the inner detector and a track segment in the muon spectrometer, with relatively little energy deposition in the calorimeters. Muon candidates are obtained by first reconstructing track segments independently in the inner detector and muon spectrometer. The muon spectrometer tracks are then back-propagated to the interaction point by modeling the effect of the detector material on the trajectory of the muon using two scattering planes and the effect on the energy using the measured or parametrized energy loss. The resulting track parameters are then compared to those of all available inner detector tracks, taking into account the uncertainties of all values; if a match is found with χ^2 probability greater than 0.001, the inner detector and muon spectrometer hits associated to the two track segments are combined in a global track refit which yields a muon candidate.

In the analysis presented here, we select muon candidates satisfying $p_{\mathrm{T}} > 20$ GeV to ensure a stable trigger efficiency. The candidates must also be reconstructed within the combined acceptance of the inner detector and muon spectrometer, corresponding to the pseudorapidity region $|\eta| < 2.5$. Since the precision of the muon transverse momentum measurement is largely determined by the inner detector track quality for p_{T} less than a few hundred GeV, we also impose several requirements on the numbers of track hits present in each subdetector, as follows.

- Pixel detector: The track must contain a hit in the innermost layer of the pixel detector, unless the relevant sensor is dead. The sum of the number of hits and number of dead sensors crossed by the track must be at least 2.

- SCT: The sum of the number of hits and number of dead sensors crossed by the track must be greater than 5.

- TRT: If $|\eta| < 1.9$, we require at least 6 hits, of which less than 90% can be outliers, i.e. they reduce the global fit quality. If $|\eta| > 1.9$ and more than 5 hits are found, then less than 90% of the hits can be outliers.

Muons coming from the semileptonic decays of charm or bottom hadrons in jets constitute an important source of background in the muon candidate sample. In order to reject these, we exploit the fact that the muons in signal events are expected to be isolated. We thus require that both the sum of the calorimeter transverse energy and the track transverse momenta in a cone of radius $\Delta R = 0.3$ around the muon direction, excluding the contributions from the muon itself, be less than 4 GeV. These variables are plotted in Figure 4.3, showing that the selected cut values achieve excellent discrimination against fake muons while keeping the acceptance for real muons high in signal events. We also veto muon candidates which are found to lie within $\Delta R < 0.4$ of any reconstructed jet with $E_{\mathrm{T}} > 20$ GeV.

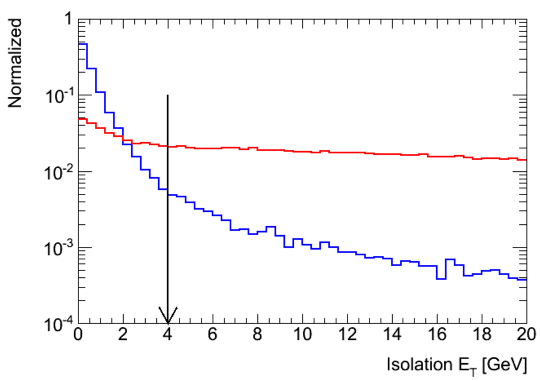

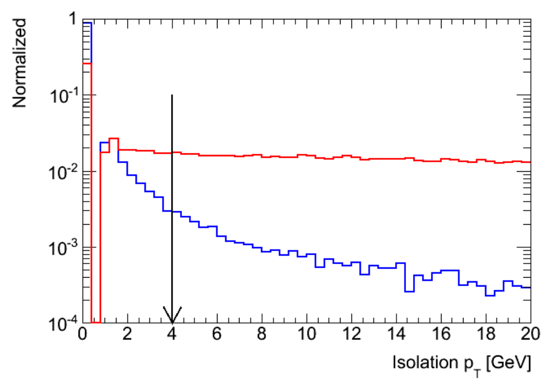

Figure 4.3: Normalized distributions for the calorimeter (left) and tracker (right) isolation variables used in muon identification. The blue and red curves are due to prompt and fake muons in simulated signal events, respectively.

4.4.4 Missing transverse energy

Missing transverse energy is used to detect the presence of high-p_{T} neutrinos in hadron collisions. At the generator level, it is simply the vector formed by taking the sum of the transverse momenta of all objects produced in the collision and reversing the direction. At the detector level, however, a more complex procedure is required. $E_{\mathrm{T}}^{\mathrm{miss}}$ in ATLAS is obtained by summing the contributions from three sources: calorimeter clusters, muons, and the cryostat correction.

The calorimeter contribution to the $E_{\mathrm{T}}^{\mathrm{miss}}$ is estimated using a refined calibration scheme. Topological clusters are first identified in the calorimeters as described in Section 4.4.2. The energy content of cluster cells is then calibrated using a set of global cell weights which depend on their energy density and location. In the final step, the cells are associated with reconstructed and identified parent objects in a specific order (electrons $\rightarrow$ jets $\rightarrow$ muons) and their energy is re-calibrated depending on their assumed identity. Cluster cells which do not match any reconstructed object are also re-calibrated by assuming that they originate from the low-energy hadronic component of the collision.

Since minimum-ionizing muons do not deposit much energy in the calorimeters, they must be treated separately in the $E_{\mathrm{T}}^{\mathrm{miss}}$ calculation. For isolated muons such as those selected in Section 4.4.3, the combined p_{T} measurement using both the inner detector and muon spectrometer information is used due to its better resolution, and any calorimeter cells assigned to the muon are removed from the calorimeter term. Muons lying within $\Delta R < 0.3$ of a reconstructed jet are handled differently: in this case, the calorimeter depositions due to the muon are indistinguishable from those of the jet, so the standalone muon p_{T} measurement from the muon spectrometer, i.e. the remaining p_{T} after the muon exits the calorimeters, is used in the $E_{\mathrm{T}}^{\mathrm{miss}}$ calculation.

Finally, the cryostat term is used to correct for any energy lost in the dead material between the electromagnetic and hadronic calorimeters, which is an important effect for high-E_{T} hadronic showers. For each reconstructed jet in the event, the correction is obtained by multiplying the cryostat calibration weight by the geometric mean of the jet energies found in the outermost layer of the electromagnetic calorimeter and the innermost layer of the hadronic calorimeter, which lie immediately in front of and behind the cryostat wall, respectively.

4.4.5 Performance

The performance of the trigger, lepton selection, and missing transverse energy reconstruction can be studied by plotting the missing transverse energy of events with a single electron or muon. This is done in Figure 4.4. The resulting distributions have a distinct two-peak structure, with the first at relatively small values of $E_{\mathrm{T}}^{\mathrm{miss}}$ and the second falling off sharply after $E_{\mathrm{T}}^{\mathrm{miss}} = 40$ GeV. The former is mainly due to hadronic events in which another object was mistakenly identified as an isolated lepton, while the latter is attributable to $W \to \ell\nu$ events, with the cutoff point corresponding roughly to $M_W/2$. At the LHC, the production of W bosons is expected to be charge asymmetric. Due to the relative importance of the $u\bar{d}$ and $d\bar{u}$ parton luminosities, we expect more W^+ bosons than W^- in proton-proton collisions. This effect is clearly seen in Figure 4.4: though the peaks due to fake leptons have similar sizes for positive and negative leptons, the W^+ peak is about 30% larger than the W^- peak for both electrons and muons, as predicted.

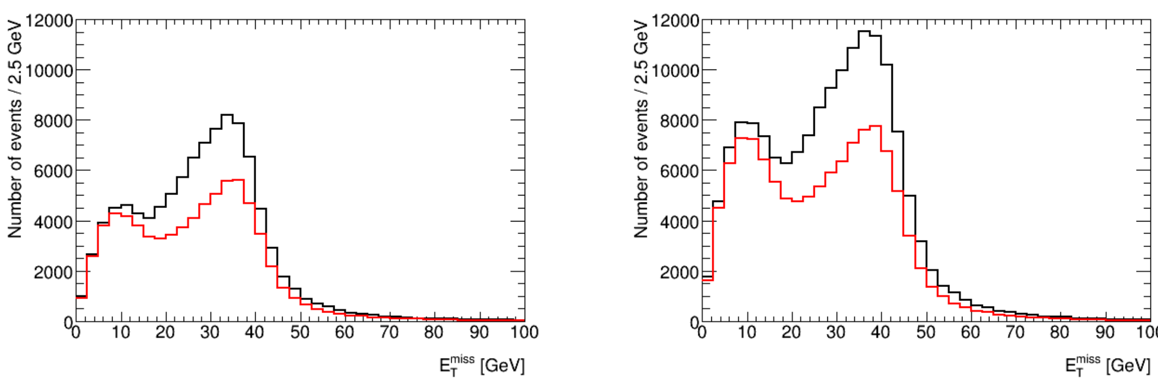

Figure 4.4: Missing transverse energy distributions in single-electron (left) and -muon (right) events, for positively- (black) and negatively- (red) charged leptons.

The performance of the trigger and lepton selection criteria can be further examined by plotting the invariant mass of lepton pairs for events having two selected electrons or muons. The result is shown in Figure 4.5. A prominent peak is visible at a mass of around 90 GeV, corresponding to events where a Z boson is produced on-shell and decays to a pair of electrons or muons. Assuming that the processes by which an object fakes an isolated lepton result in equal numbers of positively- and negatively-charged leptons, the contribution from events with one real and one misidentified lepton can be estimated by looking for dilepton events where both leptons have the same charge. As shown in Figure 4.5, very few such events are observed in data, indicating that the lepton selection used in this analysis is appropriate.

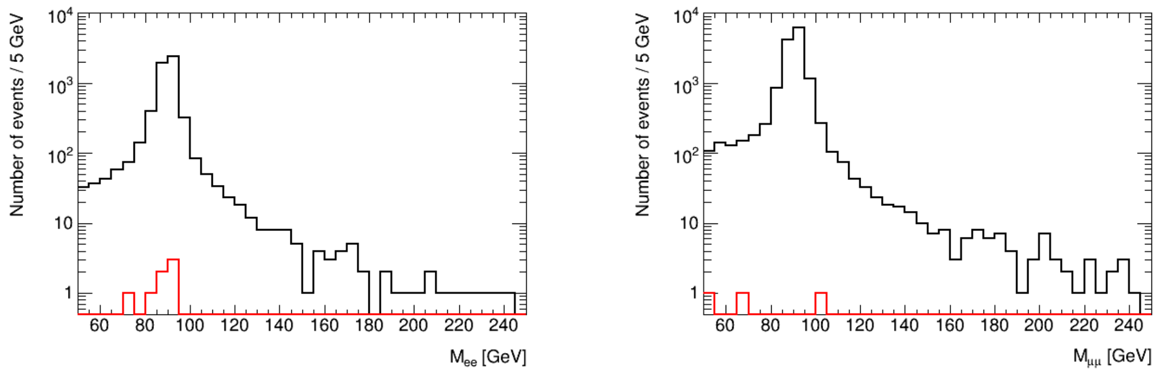

Figure 4.5: Dilepton invariant mass distributions in two-electron (left) and -muon (right) opposite-charge (black) and same-charge (red) events.

Chapter 5

Event selection

Now that the physics objects have been reconstructed and identified, the next step is to define a set of requirements on those objects that selects signal events and rejects background events with high efficiency. The composition of the resulting purified sample is then determined by estimating the contributions from signal and from each background source using simulation samples or data-driven methods.

5.1 Selection criteria

Selected events must first contain two oppositely-charged leptons. Candidates are categorized depending on the flavour combination of the selected leptons: dielectron (ee), dimuon ($\mu\mu$), or electron-muon ($e\mu$). Final states containing hadronic tau lepton decays are not used in this analysis. Events with additional loose leptons as defined in Section 5.2.2 are vetoed to ensure that events are uniquely classified in the analysis categories. Dielectron and dimuon candidate events are required to pass the unprescaled single electron and muon triggers, respectively, as described in Section 4.3. For the electron-muon category, events passing either the electron or the muon trigger (or both) are accepted, and the overlap between the two data streams is removed by requiring that muon stream events not pass the electron trigger. We also apply a trigger matching requirement to ensure that the reconstructed leptons correspond to the objects that fired the trigger: at least one of the leptons must lie within $\Delta R < 0.15$ of its trigger RoI object.

We then apply a number of general-purpose event quality requirements. In order to reject beam background events, we require that candidates contain at least one primary vertex with at least five associated tracks and veto data events with jets resulting from out-of-time energy depositions. High-p_{T} muons can sometimes undergo bremsstrahlung in the electromagnetic calorimeter, resulting in an electron-like signature; we thus veto electron-muon events where the two leptons are found to share the same inner detector track. Finally, events with a pair of anti-aligned ($\Delta\phi > 3.10$) muons having opposite-sign impact parameters are rejected if the magnitude of each impact parameter is greater than 0.5 mm; this is done to eliminate the background from cosmic rays.

In the dielectron and dimuon categories, additional cuts are required to reduce the large background from $Z \to ee$ and $Z \to \mu\mu$ events, respectively. Here, we require that the invariant mass of the lepton pair $M_{\ell\ell}$ not lie within 10 GeV of the Z boson mass and that the missing transverse energy of the event be greater than 40 GeV. For electron-muon candidates, we require that the scalar sum H_{T} of all lepton and jet transverse momenta be greater than 120 GeV.

In signal events, we expect to find a single high-p_{T} jet resulting from the hadronization of the bottom quark; if a second jet is found, it usually results from initial/final state radiation or underlying event activity, so its p_{T} is much lower. Top pair dilepton events, on the other hand, contain two top quark decays, and thus we expect two high-p_{T} jets. $Z \to \ell\ell$ and WW dilepton events usually do not contain any hard jets. The transverse momenta of the two leading jets can thus be used to discriminate against these residual backgrounds, as shown in Figure 5.1. The optimal values of the lower cut on the leading jet p_{T} and upper cut on the subleading jet p_{T} are determined by performing a two-dimensional scan and choosing the values which result in the lowest total uncertainty on the expected cross-section, accounting for all statistical and systematic uncertainties as detailed in Chapter 6. The cut values selected by this procedure are $p_{\mathrm{T}}(j_1) > 20$ GeV and $p_{\mathrm{T}}(j_2) < 30$ GeV. Note that events with exactly one reconstructed jet are considered to automatically pass the cut on the second jet p_{T}.

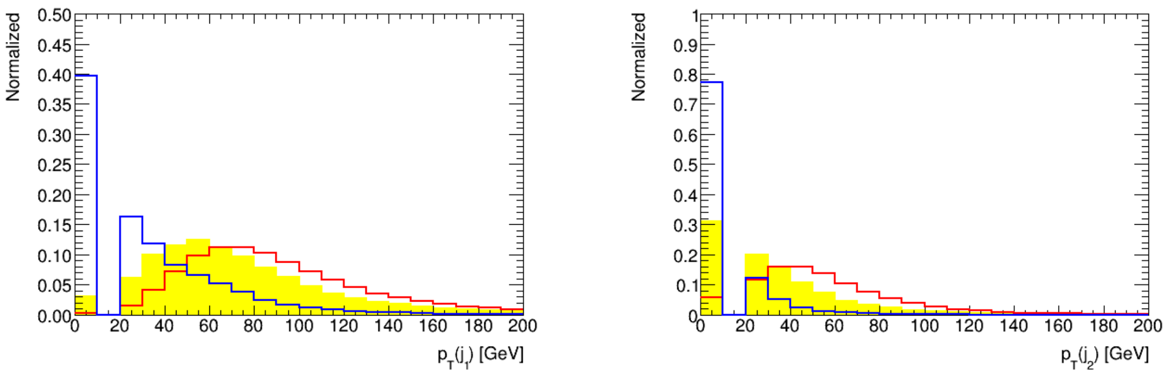

Figure 5.1: Normalized leading (left) and subleading (right) jet transverse momentum distributions for Wt signal (yellow histogram), $t\bar{t}$ background (red line), and WW background (blue line) dilepton events. The bin between 0-10 GeV contains the events where no leading/subleading jet was found.

The excellent performance of the event selection criteria is demonstrated in Table 5.1, which shows the effect of each stage of the event selection on the acceptance for signal and a few representative background processes.

5.2 Background estimates

We use the Monte Carlo simulation samples described in Section 4.2 to obtain the acceptance of the selection cuts for the Wt, $t\bar{t}$, $Z \to \tau\tau$, and diboson processes. The predicted event yields are then computed using the theoretical cross-sections of Table 4.1 and the integrated luminosity of the recorded data sample. $Z \to ee$ and $Z \to \mu\mu$ events possess no natural source of missing transverse energy, so they need to generate large fake $E_{\mathrm{T}}^{\mathrm{miss}}$ to pass our selection, for example by being produced with a high-p_{T} jet whose energy is badly mismeasured. The mechanisms by which this can occur may not be well-modeled by the simulation, so we derive the overall normalization of this background using a

Selection cut	Data	Wt	$t\bar{t}$	WW
No selection	—	1.000	1.000	1.000
Lepton selection	20,499	0.020	0.094	0.037
Trigger passed	20,242	0.020	0.093	0.036
Event quality	20,159	0.020	0.093	0.036
$M_{\ell\ell}$+$E_{\mathrm{T}}^{\mathrm{miss}}$ / H_{T}	134	0.015	0.075	0.016
Leading jet p_{T}	122	0.014	0.075	0.008
Second jet p_{T}	38	0.009	0.016	0.007

Table 5.1: Number of surviving data events and cumulative acceptance for representative processes at each step of the event selection. The starting acceptances for the $t\bar{t}$ and WW processes are higher than Wt because of the application of filters on the generated events, as detailed in Table 4.1.

data-driven technique known as the ABCD method, as described in Section 5.2.1. Finally, we cannot neglect the possibility that some object which is not an isolated lepton will nonetheless satisfy the lepton selection criteria. These "fake" isolated leptons have many possible sources, such as semileptonic charm or bottom meson decays and early photon conversions. The rates at which these various processes generate fake leptons may not be correct in the simulation, so we obtain the normalization of this background directly from data using the matrix method, as described in Section 5.2.2.

5.2.1 $Z \to ee$ and $Z \to \mu\mu$

We estimate the $Z \to ee$ and $Z \to \mu\mu$ content of the selected dielectron and dimuon samples using a data-driven procedure often referred to as the ABCD method. Independent cuts on two variables are first used to define four regions: one signal region and three background-enriched control regions. The variables used here are the invariant mass of the lepton pair and the missing transverse energy. The cut values given in Section 5.1 separate the $M_{\ell\ell} - E_{\mathrm{T}}^{\mathrm{miss}}$ plane into four regions labeled A-B-C-D, as shown in Figure 5.2. Assuming that the two variables are uncorrelated and that the control regions

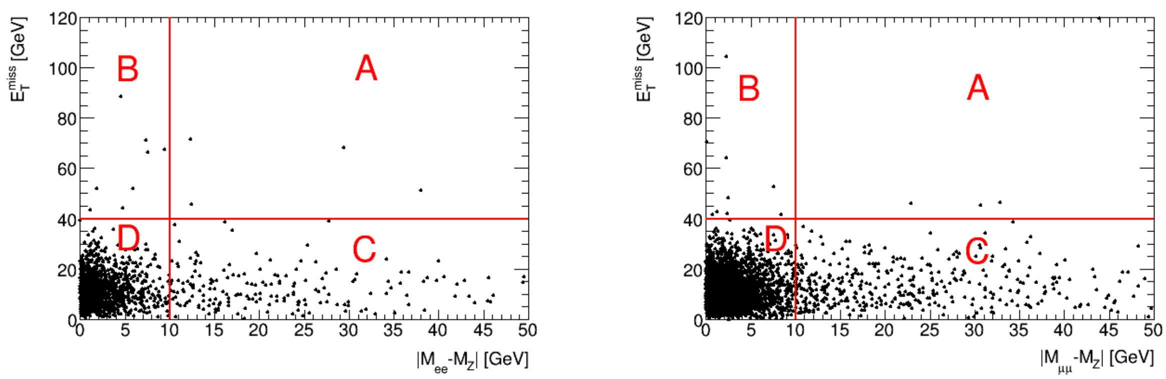

Figure 5.2: Scatter plot showing the dilepton invariant mass and missing transverse energy of all dielectron (left) and dimuon (right) data events passing the other selection criteria. The signal and control regions used in the ABCD method are clearly indicated.

B-C-D only contain $Z \to ee$ or $Z \to \mu\mu$ events, the contribution of that background to the signal region A is simply $N_A = N_C \times N_B/N_D$. However, there is non-negligible contamination from other processes such as $t\bar{t}$, Wt, $Z \to \tau\tau$, and dibosons — up to 25% in region B — which we estimate using the MC simulation samples and subtract from the observed data numbers as in Equation 5.1.

$$N_A = (N_C^{\mathrm{data}} - N_C^{\mathrm{MC,non-Z}}) \times \frac{N_B^{\mathrm{data}} - N_B^{\mathrm{MC,non-Z}}}{N_D^{\mathrm{data}} - N_D^{\mathrm{MC,non-Z}}} \tag{5.1}$$

Note that the non-Z background subtraction introduces some circularity in the analysis, as the cross-section of interest is used to normalize the Wt event yields in the $Z \to \ell\ell$ control regions. However, the background from Wt events is extremely small, and it was verified that this has a negligible effect on the final result.

5.2.2 Fake leptons

A data-driven technique known as the matrix method is used to obtain the estimate of the fake lepton background component of the selected sample. We first define a looser identification level for both electron and muons by dropping some of the requirements introduced in Sections 4.4.1 and 4.4.3. For electrons, we loosen the isolation requirements and the track and shower shape cuts, while for muons, the calorimeter and tracker isolation cuts are dropped.

The next step is to measure the rates at which real and fake loose leptons pass the default ("tight") identification using control regions purified in real and fake leptons. For real leptons, we use a purified sample of Z boson events obtained by requiring one tight and one oppositely-charged loose lepton whose invariant mass lies within 5 GeV of the Z boson mass. For fake leptons, the efficiency is measured using events with a single loose lepton, at least one jet, and low missing transverse energy. The results are shown in Figure 5.3. We find efficiencies for real and fake electrons of $r_e = 0.809 \pm 0.004$ and $f_e = 0.1091 \pm 0.0008$, respectively, where the quoted uncertainty is only statistical. The results for real and fake muons are $r_\mu = 0.9921 \pm 0.0006$ and $f_\mu = 0.440 \pm 0.002$, respectively. The difference between the electron and muon fake efficiencies is mostly attributable to the muon-jet overlap cut which is part of the loose muon selection: as the loose muons are already required to be located far from any calorimeter energy deposits, they have a higher chance to satisfy the isolation cuts of the tight selection.

The sample formed by data events having two loose leptons can then be subdivided into four categories, depending on whether or not each lepton also satisfies the tight lepton selection; the resulting categories are referred to as tight-tight (TT), tight-loose (TL), loose-tight (LT), and loose-loose (LL). On the other hand, the same events can also be classified depending on whether the two lepton candidates come from real or fake leptons; this yields four new categories known as real-real (RR), real-fake (RF), fake-real (FR), and fake-fake (FF). These two compositions are related by Equation 5.2, where r_i

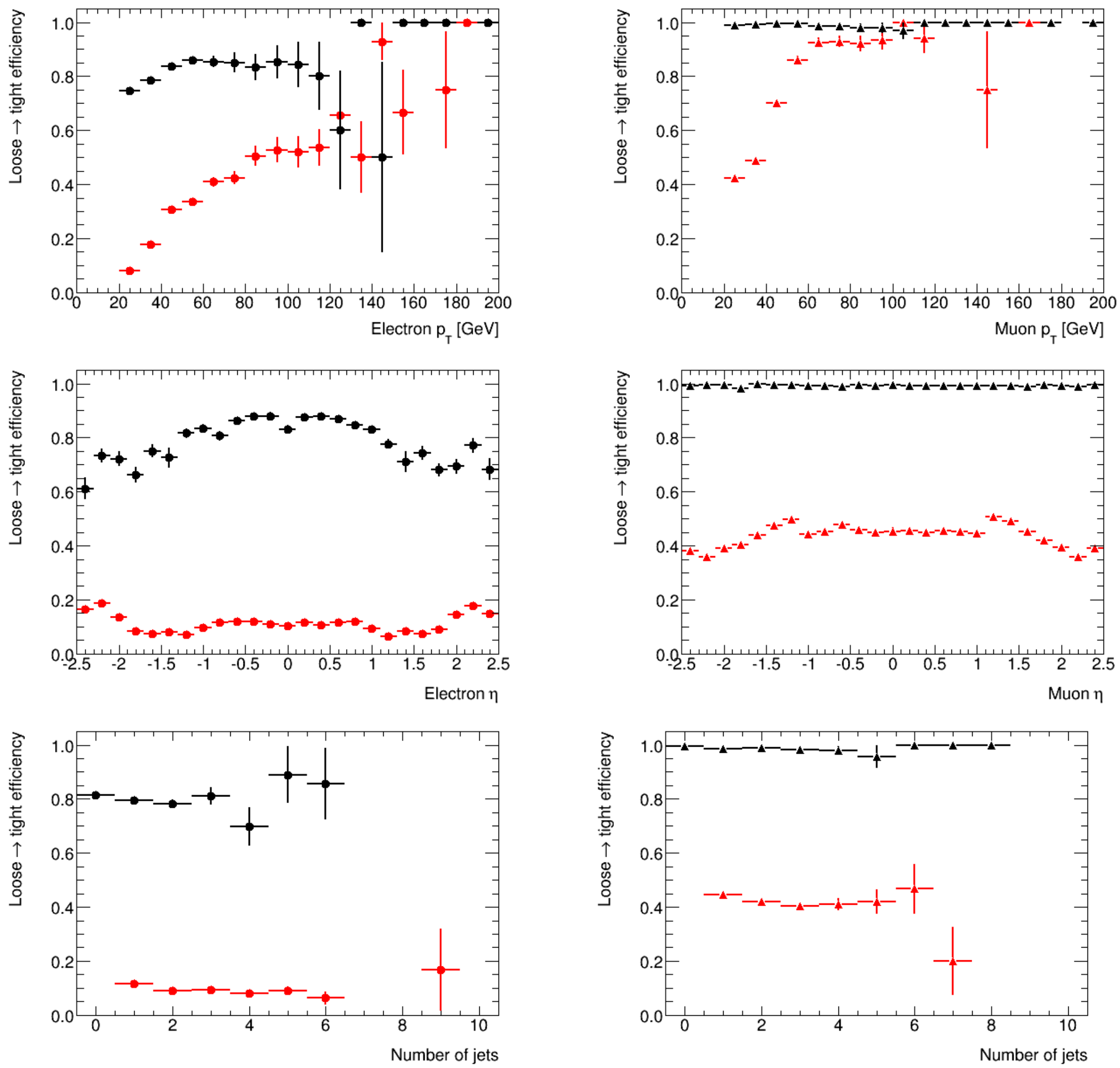

Figure 5.3: Measured loose-to-tight efficiencies for real (black) and fake (red) electrons (left) and muons (right) versus lepton transverse momentum, lepton pseudorapidity, and number of reconstructed jets.

and f_i are the measured real and fake efficiencies for each lepton type.

$$\begin{bmatrix} N_{TT} \\ N_{TL} \\ N_{LT} \\ N_{LL} \end{bmatrix} = \begin{bmatrix} r_1 r_2 & r_1 f_2 & f_1 r_2 & f_1 f_2 \\ r_1(1-r_2) & r_1(1-f_2) & f_1(1-r_2) & f_1(1-f_2) \\ (1-r_1)r_2 & (1-r_1)f_2 & (1-f_1)r_2 & (1-f_1)f_2 \\ (1-r_1)(1-r_2) & (1-r_1)(1-f_2) & (1-f_1)(1-r_2) & (1-f_1)(1-f_2) \end{bmatrix} \begin{bmatrix} N^{RR} \\ N^{RF} \\ N^{FR} \\ N^{FF} \end{bmatrix} \tag{5.2}$$

The composition of the sample of interest, in which both leptons are required to pass the tight selection, is derived by making the following variable substitutions:

$$\begin{aligned} N_{TT}^{RR} &= r_1 r_2 N^{RR} \\ N_{TT}^{RF} &= r_1 f_2 N^{RF} \\ N_{TT}^{FR} &= f_1 r_2 N^{FR} \\ N_{TT}^{FF} &= f_1 f_2 N^{FF}, \end{aligned}$$

then inverting the matrix. This yields Equation 5.3. The fake lepton background estimate used in the next section is then simply obtained from $N_{\text{fake}} = N_{TT}^{RF} + N_{TT}^{FR} + N_{TT}^{FF}$.

$$\begin{bmatrix} N_{TT}^{RR} \\ N_{TT}^{RF} \\ N_{TT}^{FR} \\ N_{TT}^{FF} \end{bmatrix} = \frac{1}{(r_1-f_1)(r_2-f_2)} \begin{bmatrix} r_1 r_2(1-f_1)(1-f_2) & -r_1 r_2(1-f_1)f_2 & -r_1 r_2 f_1(1-f_2) & r_1 r_2 f_1 f_2 \\ -r_1 f_2(1-f_1)(1-r_2) & r_1 f_2(1-f_1)r_2 & r_1 f_2 f_1(1-r_2) & -r_1 f_2 f_1 r_2 \\ -f_1 r_2(1-r_1)(1-f_2) & f_1 r_2(1-r_1)f_2 & f_1 r_2 r_1(1-f_2) & -f_1 r_2 r_1 f_2 \\ f_1 f_2(1-r_1)(1-r_2) & -f_1 f_2(1-r_1)r_2 & -f_1 f_2 r_1(1-r_2) & f_1 f_2 r_1 r_2 \end{bmatrix} \begin{bmatrix} N_{TT} \\ N_{TL} \\ N_{LT} \\ N_{LL} \end{bmatrix} \tag{5.3}$$

5.3 Event yields and kinematic distributions

The composition of the selected sample is detailed in Table 5.2. Combining all three lepton categories, we expect 38.6 ± 6.0 events to survive the selection, including 4.3 ± 0.3 signal events. Our selection results in signal-to-background ratios of 9%, 15%, and 13% in the dielectron, dimuon, and electron-muon channels, respectively. It is interesting to see that the dimuon channel achieves a greater S/B than the electron-muon channel, despite having an important additional source of background in $Z \to \mu\mu$+jets events; this is due to the large rate of events with one real muon and one fake electron passing the event selection. We observe 38 events passing the selection in the ATLAS 2010 dataset, consistent with expectations.

Process	$e\mu$	ee	$\mu\mu$
Wt	2.4 ± 0.2	0.5 ± 0.1	1.4 ± 0.1
$t\bar{t}$	10.3 ± 2.0	2.1 ± 0.7	$5.1^{+0.8}_{-1.2}$
$Z \to ee$	—	1.4 ± 0.8	—
$Z \to \mu\mu$	—	—	$1.2^{+1.3}_{-0.9}$
$Z \to \tau\tau$	2.3 ± 0.9	0.5 ± 0.4	1.4 ± 0.6
WW	2.5 ± 0.3	0.5 ± 0.1	1.5 ± 0.2
WZ	0.27 ± 0.02	0.10 ± 0.01	0.30 ± 0.05
ZZ	0.041 ± 0.004	0.023 ± 0.003	0.14 ± 0.03
Fake leptons	3.7 ± 2.4	0.8 ± 0.6	$0.0^{+0.7}_{-0.0}$
Total background	19.1 ± 3.4	5.4 ± 1.3	9.6 ± 1.9
Total expected	21.5 ± 3.5	5.9 ± 1.3	11.1 ± 1.9
Observed	24	6	8

Table 5.2: Expected and observed event yields in the selected Wt sample. Uncertainties represent the combined effect of all statistical and systematic uncertainties as described in Chapter 6.

Distributions of relevant kinematic variables are shown in Figures 5.4, 5.5, and 5.6 for the dielectron, dimuon, and electron-muon samples, respectively. In these plots, the shape of the $Z \to ee$ and $Z \to \mu\mu$ backgrounds is obtained by renormalizing the predictions obtained from the ALPGEN Monte Carlo samples of Table 4.1 to the ABCD method prediction, whereas the shape of the fake lepton background is taken from events passing the full event selection, but where one of the leptons only satisfies the loose criteria. Good agreement is found between the predicted and observed shapes, within the large statistical uncertainties.

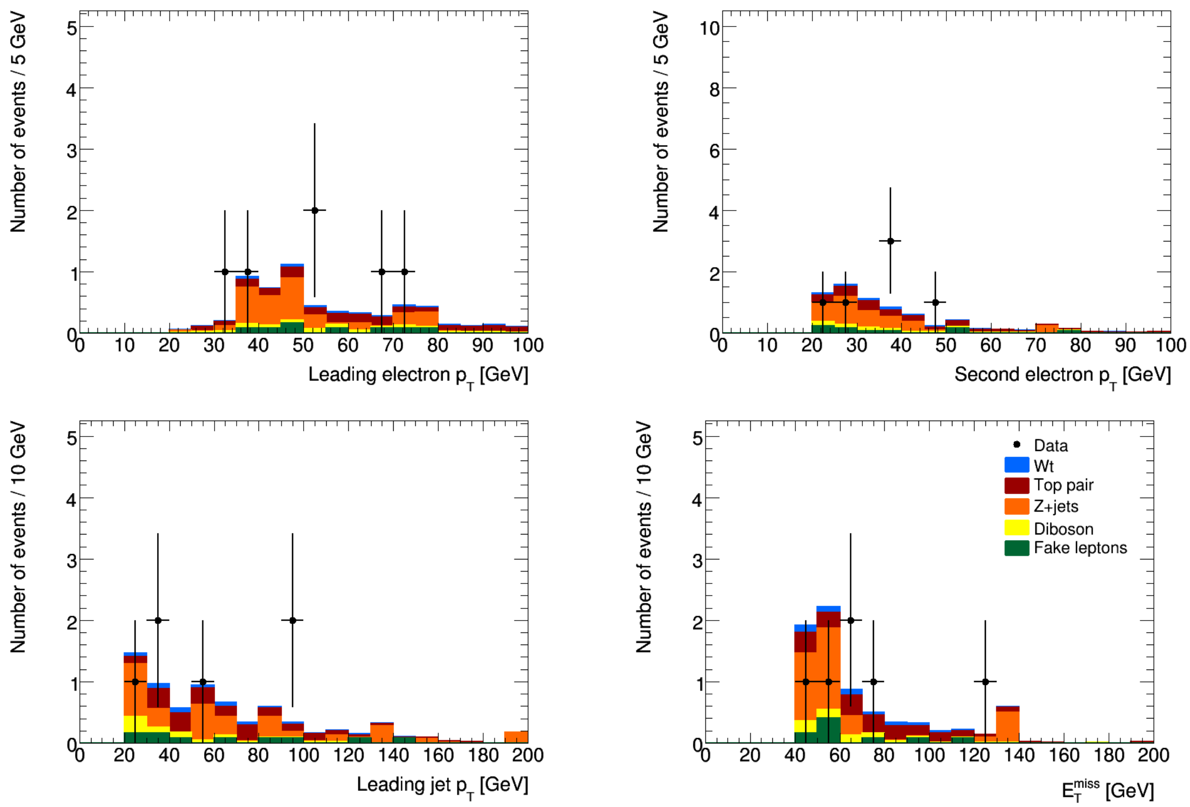

Figure 5.4: Kinematic variable distributions for the selected dielectron sample.

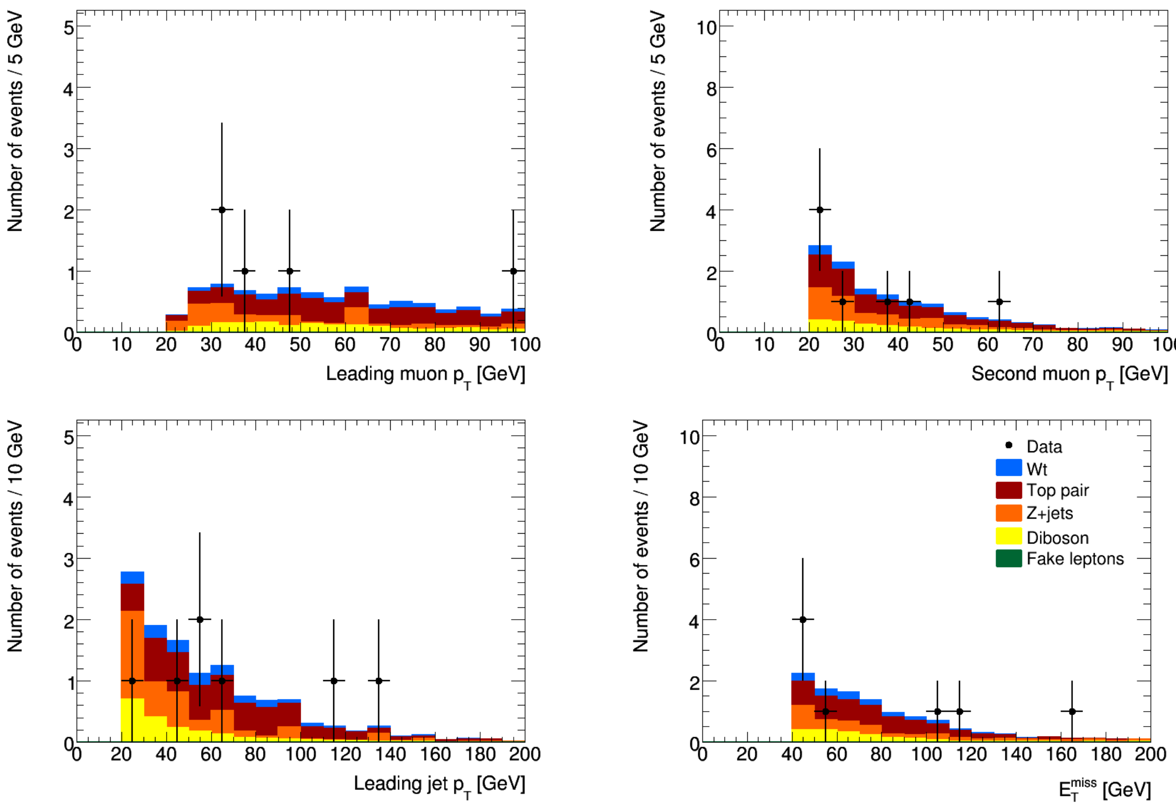

Figure 5.5: Kinematic variable distributions for the selected dimuon sample.

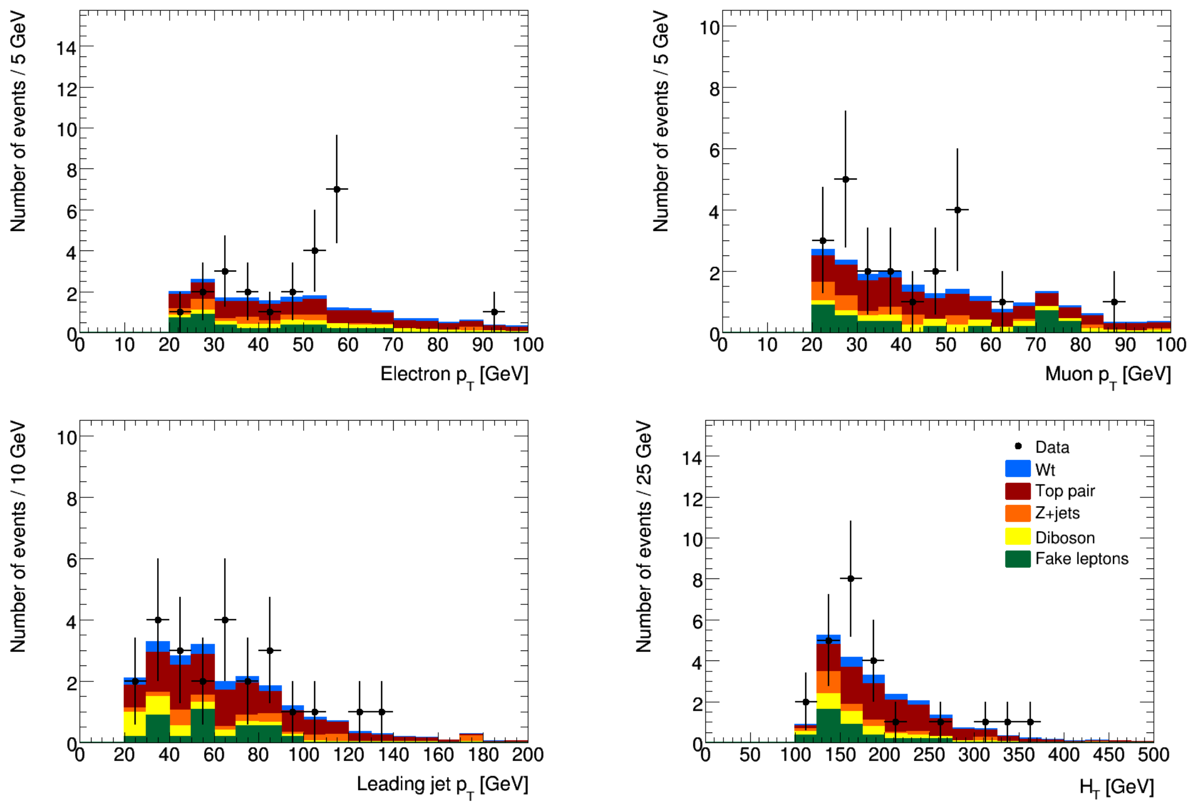

Figure 5.6: Kinematic variable distributions for the selected electron-muon sample.

Chapter 6

Cross-section extraction

In this chapter, the purified signal sample obtained in the previous section is used to extract a measurement of the parameter of interest in this analysis, namely the cross-section for Wt-channel single top quark production. We first describe the procedure used to obtain the measured cross-section value and propagate the effect of statistical and systematic uncertainties from the event yield predictions to the cross-section measurement, then discuss the various sources of systematic uncertainty affecting the measurement. Finally, we unveil the result and derive an upper limit on the production of Wt-channel single top quark events.

6.1 Propagation of uncertainties

The most direct way to extract the cross-section for some physical process of interest from a selected sample of events is through Equation 6.1.

$$\sigma = \frac{N - B}{\epsilon_S \mathcal{L}} \tag{6.1}$$

The difference between the number of surviving data events N and the sum of the predicted background yields B is assumed to be due to the presence of signal events, where the background term can include both data- and MC- driven predictions. The latter are obtained through $B_i = \epsilon_i \sigma_i \mathcal{L}$, where ϵ_i is the product of the acceptance and efficiency from the MC sample (henceworth simply referred to as the acceptance), σ_i is the theoretical cross-section, and $\mathcal{L}$ represents the measured integrated luminosity. The signal cross-section is then obtained by dividing the number of signal events $N - B$ by the product of the signal acceptance ϵ_S, as extracted from the signal simulation sample, and the measured integrated luminosity $\mathcal{L}$.

In order to simplify the treatment of the uncertainties, however, we opt for an approach based on maximum-likelihood estimation. The three analysis channels are combined into a single likelihood function, shown in Equation 6.2, which is then maximized to obtain the optimal value of the signal cross-section.

$$L(\sigma, \alpha_j) = \prod_i \frac{\left[S_i\left(\sigma, \alpha_j\right) + B_i\left(\alpha_j\right)\right]^{N_i}}{N_i!} e^{-\left[S_i(\sigma,\alpha_j)+B_i(\alpha_j)\right]} \times \prod_j \frac{1}{\sqrt{2\pi}} e^{-\alpha_j^2/2} \tag{6.2}$$

This is equivalent to finding the minimum value of the negative log-likelihood (shown in Equation 6.3 up to constant terms) within the full parameter space.

$$-\log L(\sigma, \alpha_j) = \sum_i \left[S_i\left(\sigma, \alpha_j\right) + B_i\left(\alpha_j\right)\right] - N_i \log\left[S_i\left(\sigma, \alpha_j\right) + B_i\left(\alpha_j\right)\right] + \sum_j \alpha_j^2/2 \tag{6.3}$$

For each channel i, the likelihood function includes a Poisson term in the observed number of events N_i with expectation value $S_i + B_i$, which is the sum of the expected contributions from signal ($S_i = \epsilon_S \sigma \mathcal{L}$) and all MC- or data-driven backgrounds. Systematic uncertainties are grouped into uncorrelated sets j and their effect is parametrized using a set of nuisance parameters α_j, where $\alpha_j = 0$ maps to the nominal value and $\alpha_j = \pm 1$ map to the single standard deviation shifts of the affected parameters. The nuisance parameter probability density functions are embedded directly into the likelihood function, in an approach sometimes called 'floating systematics': for each α, a Gaussian term is multiplied into the likelihood function. This effectively constrains the nuisance parameter values by reducing the likelihood whenever a nuisance parameter goes off-peak, corresponding to $\alpha \neq 0$. Piecewise-linear interpolation is used to propagate the effect of the α_j to the expected signal and background yields. This approach has a number of advantages compared to methods based on generating large numbers of pseudoexperiments: it is much more computationally economical and treats the nuisance parameters on the same footing as the parameter of interest in the fit.

The effect of the uncertainty from data statistics is evaluated by forming the likelihood ratio: all of the α nuisance parameters are fixed to zero, and the quantity $\lambda(\sigma) = L(\sigma)/L(\hat{\sigma})$ (or $-\log\lambda(\sigma)$) is computed for the full range of possible cross-section values, where $\hat{\sigma}$ is the maximum likelihood estimate (MLE) for the signal cross-section. To add the effect of systematics uncertainties, we form the profile likelihood ratio $\lambda(\sigma) = L(\sigma, \hat{\hat{\alpha}}_j)/L(\hat{\sigma}, \hat{\alpha}_j)$, where a single circumflex represents the global MLE over the full parameter space and the double circumflex represents the conditional MLE with σ fixed to the test hypothesis.

6.2 Systematic uncertainties

6.2.1 Integrated luminosity

The integrated luminosity of the data sample is needed to convert the MC sample acceptances into expected signal and background yields. In ATLAS, this quantity is monitored by several subdetectors and is occasionally calibrated to the absolute luminosity provided by the LHC using specialized runs known as van der Meer scans. The total uncertainty on the integrated luminosity determination is 3.4% [45, 46], most of which arises from the residual uncertainty on the LHC bunch currents.

6.2.2 Object performance

Differences between the actual and simulated detector performance naturally lead to biases in the MC-predicted event yields. We rectify these discrepancies at the object selection stage, first by scaling or smearing the energies of the objects to reproduce the distributions seen in data control samples, and second by applying data/MC scale factors to account for any difference in the trigger, reconstruction, or identification efficiencies.

For electrons and muons, purified samples of $Z \to ee$ and $Z \to \mu\mu$ decays are used to determine these corrections. The efficiencies in data and MC are measured using the tag-and-probe method: events containing one selected object (the tag) and one candidate object (the probe) with an invariant mass close to that of the Z boson form the denominator, and the numerator is obtained by requiring that the probe also pass the criteria of interest. The energy scale and resolution corrections are obtained by determining the parameter values which result in the best agreement between the shapes of the Z boson mass peak seen in data and simulation. These corrections have associated uncertainties arising from the limited Z boson statistics in data as well and the presence of non-Z events in the control sample.

The electron trigger and reconstruction scale factors are measured to be 0.995 ± 0.005 and 1.000 ± 0.015 respectively, with no significant dependence observed on the kinematic variables of the electron candidate. The electron identification scale factors, on the other hand, are measured in 6 bins of E_{T} and 8 bins of pseudorapidity, the results varying between 0.908 ± 0.082 and 1.061 ± 0.036. An η-dependent energy scale offset correction is applied to the data, while the energy resolution correction is applied to the simulation samples.

The muon trigger scale factors are measured in 10 $\eta - \phi$ bins and range between $0.843^{+0.053}_{-0.055}$ and $1.046^{+0.031}_{-0.030}$. We also apply an overall reconstruction and identification scale factor of 0.999 ± 0.004 on the Monte Carlo results. The p_{T} scale and resolution corrections are applied separately to the inner detector and muon spectrometer tracks in the simulation, then propagated to the combined muon candidates.

The jet uncertainties are treated differently, since the jet energy scale applied to both the data and simulation is derived from simulation results. The uncertainty on the jet energy scale thus arises from possible biases present in the simulation, and is evaluated using a combination of data- and MC-based techniques. The total uncertainty is found to be less than 4.5% (2.5%) for central jets with $p_{\mathrm{T}} < 60$ GeV ($60 < p_{\mathrm{T}} < 800$ GeV). The effect of this uncertainty on our predicted event yields is obtained by scaling the energies of all jets up or down by one standard deviation of the scale uncertainty, then reapplying the event selection. We also apply additional smearing to the simulated jet energies to replicate the energy resolution observed in data; the uncertainty due to this effect is obtained by symmetrizing the difference between the acceptances measured from the smeared and unsmeared simulation samples. Finally, the uncertainty due to the difference between the jet reconstruction efficiency in data and simulation is evaluated by randomly dropping jets from simulated events depending on their p_{T} and $|\eta|$.

The missing transverse energy calculation mostly relies on associating calorimeter clusters to reconstructed objects, so we propagate the electron, muon, and jet energy corrections, along with their associated uncertainties, to the $E_{\mathrm{T}}^{\mathrm{miss}}$ calculation. The only exceptions are the contributions to $E_{\mathrm{T}}^{\mathrm{miss}}$ from soft ($7 < p_{\mathrm{T}} < 20$ GeV) jets and clusters which are not associated with any reconstructed objects. We associate 10.5% and 13.2% scale uncertainties to these two components, respectively, which we assume to be uncorrelated to the other systematic uncertainties [47].

6.2.3 Data-driven background estimates

The data-driven techniques used in Sections 5.2.1 and 5.2.2 to estimate the $Z \to ee/Z \to \mu\mu$ and fake lepton components of the selected sample are not affected by the other items discussed in this section, but they do have their own sources of both statistical and systematic uncertainty.

In the ABCD method, the statistical uncertainty is due to the limited numbers of data events which populate the $Z \to \ell\ell$ control regions, while systematic effects arise from the MC-based background subtraction procedure and imperfect knowledge of the $E_{\mathrm{T}}^{\mathrm{miss}}$ scale. The statistical uncertainty is evaluated by performing pseudoexperiments in which the number of data events in each control region is randomly shifted about the observed value. To evaluate the impact of the background subtraction uncertainty, we shift all MC estimates up and down by 20% and recompute the predictions. As most of the contamination comes from top pair events, whose theoretical cross-section is known to better than 10%, this is considered a conservative approach. Finally, we also check the stability of the predictions against changes in the $E_{\mathrm{T}}^{\mathrm{miss}}$ scale by changing the $E_{\mathrm{T}}^{\mathrm{miss}}$cut used to define the control regions to 35 GeV and 45 GeV. These three sources are assumed to be uncorrelated in the calculation of the total uncertainty.

The matrix method, on the other hand, suffers from statistical limitations in two respects: first, the number of data events in the control regions used to measure the real and fake loose-to-tight efficiencies is finite, and second, the observed composition of the loose-loose sample which appears on the right side of Equation 5.3 is also subject to statistical fluctuations. Systematic effects affecting the predictions include the possible biases caused by the lack of parametrization of the real and fake efficiencies and the residual contamination of the control regions. We conservatively assign an uncertainty corresponding to 50% of the greater of the yield prediction or its statistical uncertainty to account for these effects; this value was chosen because it amply covers the differences between the predictions obtained with the matrix method and other independent techniques.

6.2.4 Background cross-sections

Theoretical cross-section predictions are used to compute the event yields from the MC sample acceptances for the $t\bar{t}$, $Z \to \tau\tau$, and diboson processes. These values are of course finite order results, and thus have associated systematic uncertainties. For top pair production, we use the error on the approximate NNLO result as presented in Section 2.2, corresponding to a relative uncertainty of $^{+7.0\%}_{-9.6\%}$. The theoretical cross-sections for the diboson processes are slightly better understood in theory, so we use an uncertainty of ±5%. These values include the contributions from the renormalization/factorization scale choice as well as the choice of parton distribution functions. Finally, for the exclusive $Z \rightarrow \tau\tau$ MC samples, since the theoretical predictions are better for low jet multiplicities, we associate different uncertainties depending on the number of produced partons. The exclusive 0-jet cross-section is known to a precision of 4% from theory; for each additional outgoing parton, a 24% uncertainty is added in quadrature to account for the theoretical uncertainty on the ratio of $(n+1)/n$-parton production [48], resulting in 24%, 34%, 42%, 48%, and 54% uncertainties for the 1, 2, 3, 4, and 5 parton samples, respectively.

6.2.5 Generator choice

As seen in Section 4.2, there exists a wide variety of event generation software. Each program is based on a different model of hard scattering interactions and thus produces slightly different predictions. These model choices may introduce some bias in the event yield predictions. This effect is quantified for the top pair background, which constitutes most of the selected sample, by comparing the nominal results with those obtained from alternate MC samples generated with different matrix element and parton shower software choices. The nominal sample uses the MC@NLO generator and HERWIG parton shower model; alternate samples are produced with the POWHEG [49, 50, 51] generator and HERWIG or PYTHIA [52] parton shower models.

6.2.6 Initial/final state radiation modeling

Emission of additional partons by the initial or final state particles is referred to as initial or final state radiation, accordingly. The software used to produce our MC samples simulates these subprocesses by relying on theoretically-motivated models whose parameters are tuned to best match a set of experimental observations. We quantify this uncertainty for the Wt signal and $t\bar{t}$ background processes using a set of customized MC samples produced with the leading-order generator AcerMC [53] version 3.5 interfaced with PYTHIA, in which the PYTHIA parameters which govern initial and final state radiation have been varied to explore the full experimentally-allowed parameter space.

6.2.7 Parton distribution functions

Parton distribution function (PDF) sets are used to bridge the gap between the theoretical calculations of the parton-level hard processes and the hadron collisions generated at the LHC. Each set provides the probability density functions for observing each type of parton at each value of momentum fraction x in hadron collisions. These are obtained by fitting a large collection of experimental data using some assumed parametrization for each partonic component. Various collaborations produce PDF sets, each using its own parametrizations and preferred set of experimental results. Here, PDF sets are needed both in the derivation of the theoretical cross-sections and in the event generation; the uncertainty from the first source was already discussed in Section 6.2.4, while the latter is obtained from the following procedure. First, we recompute the event yield predictions after varying each fit parameter up and down by one standard deviation, resulting in $2n$ values, where n is the number of parameters. This is done for three different PDF sets: CTEQ66, MSTW2008 [54], and NNPDF20 [55]. The uncertainty due to the choice of PDF set is then taken to be the difference between the maximum and minimum acceptance seen from the variations in all three PDF sets.

6.3 Results

The measured cross-section and its uncertainties are inferred from the shapes of the likelihood ratio and profile likelihood ratio curves. As shown in Figure 6.1, we extract both the expected and observed cross-section measurements, where the former are obtained by setting $N_i = S_i + B_i$ for all i in Equation 6.2. Accounting for all sources of statistical and systematic uncertainty, we measure the cross-section for Wt-channel single top quark

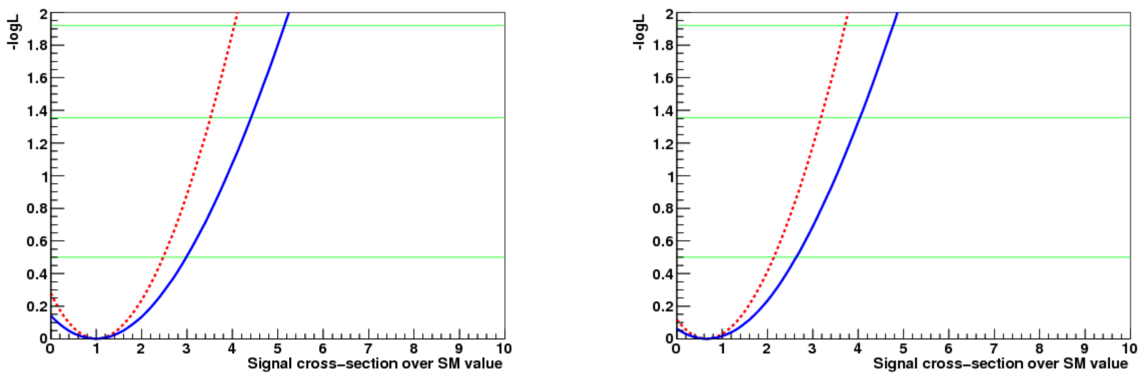

Figure 6.1: Likelihood ratio (red dashed) and profile likelihood ratio (blue solid) curves for the expected (left) and observed (right) cross-section measurements.

production to be

$$\sigma(pp \to Wt) = 10\ ^{+20}_{-10}\ (\text{stat})\ ^{+20}_{-10}\ (\text{syst})\ \text{pb}.$$

Assuming the Standard Model cross-section for Wt production with a top quark mass of 172.5 GeV, the expected cross-section value is

$$\sigma(pp \to Wt) = 15\ ^{+22}_{-15}\ (\text{stat})\ ^{+19}_{-15}\ (\text{syst})\ \text{pb}.$$

The full breakdown of the uncertainty on the expected measurement is provided in Table 6.1. As was already obvious from the paltry signal event yields shown in Section 5.3, this measurement is heavily statistically limited — however, systematic uncertainties contribute an almost equal amount to the total uncertainty. The dominant sources of systematic uncertainty are the fake lepton background determination and the theoretical cross-section uncertainties for the MC-driven processes. The modeling of initial and final state radiation also has a large effect on the signal and $t\bar{t}$ yield predictions. This measurement is still much too statistically limited to approach the level of evidence or discovery, so we use the data to set an upper limit on the anomalous Standard-Model-like production of Wt events. Assuming that $-2\log\lambda(\sigma)$ is χ^2-distributed, a two-sided 95% confidence interval is formed by the cross-section values satisfying $-2\log\lambda(\sigma) \leq 3.84$. We quote the upper bound of this interval as the upper limit on the production cross-

Source	$\Delta\sigma/\sigma$ [%]
Data statistics	+148/-100
MC statistics	+24/-28
Luminosity	+29/-20
Electron performance	+23/-16
Muon performance	+14/-15
Jet performance	+39/-26
$E_{\mathrm{T}}^{\mathrm{miss}}$ performance	+2/-2
$Z \to \ell\ell$ background estimation	+23/-37
Fake lepton background estimation	+61/-79
Background cross-sections	+65/-62
Generator choice	+34/-36
Initial/final state radiation	+54/-38
Parton distribution functions	+32/-30
All systematics	+136/-100
Total uncertainty	+200/-100

Table 6.1: Breakdown of the relative uncertainty on the expected Wt-channel cross-section.

section. Due to the boundary at $\sigma = 0$, the χ^2 assumption is not strictly valid in this case; however, for this analysis the resulting deviation is very small and neglecting this effect only results in a small level of conservatism in the limit [56]. The observed limit is $\sigma(pp \to Wt) < 4.8 \times \sigma_{\mathrm{SM}} = 70$ pb.

Chapter 7

Conclusion

In the Standard Model of particle physics, the electroweak production of single top quarks proceeds through three distinct production modes, known as t-channel, s-channel, and Wt-channel; the first two processes were observed by the CDF and D0 collaborations in 2009, while the third is not accessible in the Tevatron's proton-antiproton collisions. In this thesis, we have presented the first search for Wt-channel single top quark production. This search was based on proton-proton collision data taken at a center-of-mass energy of 7 TeV with the ATLAS experiment at the Large Hadron Collider between June and October 2010, corresponding to a total integrated luminosity of 35 pb^{-1}. An event selection requiring two oppositely-charged leptons, a single high-p_{T} jet, and high missing transverse energy or total transverse energy was used to obtain purified samples of Wt-channel single top events. The composition of these samples was estimated using Monte Carlo simulation samples of relevant physical processes or, where some aspect of the simulation may not be correctly modeled, data-driven techniques. We found 38 data events surviving the selection in data compared to a total prediction of 38.6 ± 6.0, with a resulting signal-to-background ratio of 0.13. A statistical technique based on maximum likelihood estimation was used to propagate the effect of the statistical and systematic uncertainties from the predicted event yields to the Wt-channel cross-section measurement.

The measured cross-section value is $\sigma(pp \rightarrow Wt) = 10\,^{+20}_{-10}\,(\text{stat})\,^{+20}_{-10}\,(\text{syst}) = 10\,^{+28}_{-10}$ pb. The significance of the background-only hypothesis was found to be insufficient to claim evidence or discovery, so we derive a 95% confidence level upper limit on the parameter of interest of $\sigma(pp \rightarrow Wt) < 70$ pb.

As with all single top analyses, the main challenge in searching for Wt production was to find a set of selection criteria which suppresses the large backgrounds from gauge boson production and top quark pair production. Here, we opted for a simple approach that used the transverse momenta of the two leading jets as the main discriminating variables. Potential improvements to this analysis could come both from the addition of new discriminating variables and from the combination of many variables into a single discriminant using sophisticated tools such as boosted decision trees or neural networks. Events having a second high-p_{T} jet were vetoed in this analysis, but the signal acceptance could be increased by finding new discriminating variables for these events, for example taking advantage of the expected energy imbalance between the two hemispheres of the event as defined by the leading jet direction. The application of a b-tagging veto on the subleading jet would also be a powerful tool in suppressing the top pair background in events with multiple high-p_{T} jets. The search for the Wt-channel process could also be performed in the lepton+jets final states, but the large backgrounds from top pair production and W+jets events make that particular analysis even more challenging.

Wt-channel single top quark production is very likely to be the first major discovery made by the LHC experiments in proton-proton collisions. With the astounding rate at which the LHC is now delivering collisions to the ATLAS and CMS detectors, this should become possible by the end of 2011. In the longer term, the large dataset expected from the LHC should make precision studies of the electroweak interactions of top quarks possible, including measurements of the cross-sections of all three single top processes. This will provide another valuable test of Standard Model predictions and should allow us to constrain a wide range of new physics models.

Appendix A

Measurement of the top quark pair production cross-section with Z boson normalization

In this appendix, I describe a new technique for performing cross-section measurements in which all dependence on the integrated luminosity and its uncertainty is eliminated from the measurement. This is achieved by adding a second parallel cross-section analysis in which the theoretical cross-section for the signal process is used to achieve an in-situ normalization of the event yields for the common dataset. This method was originally expected to vastly improve the precision of cross-section measurements in ATLAS and was intended to be the focus of this thesis; however, due to the unprecedented precision achieved by the ATLAS integrated luminosity measurement, its performance was found to be merely comparable to that of the standard cross-section measurement procedure. Nevertheless, it does provide a valuable cross-check with different sources of systematic uncertainty.

Recall from Equation 6.1 that generally, the cross-section of any physical process can be measured by defining a sample of purified signal events, subtracting the predicted background contributions from the observed event yields, then dividing the result by the signal acceptance and integrated luminosity. However, if a theoretical cross-section prediction is available for the signal process, the same equation can be inverted to yield a measurement of the integrated luminosity, as shown in Equation A.1. Physics processes such as inclusive W or Z boson production, for which precise theoretical predictions are available, can thus be used to measure or monitor the integrated luminosity delivered to an experiment. This possibility was mentioned in the ATLAS technical proposal [57].

$$\mathcal{L} = \frac{N - B}{\epsilon_S \sigma_{\text{theo}}} \tag{A.1}$$

Alternatively, if the cross-sections for two different physical processes are measured using the same dataset, the ratio of those values is almost independent of the integrated luminosity, as shown in Equation A.2. The cross-section for the process of interest can then simply be extracted by multiplying the measured ratio by the theoretical prediction for the second process, $\sigma_1 = R \times \sigma_{2,\text{theo}}$.

$$R = \frac{\sigma_1}{\sigma_2} = \frac{\frac{N_1 - B_1}{\epsilon_1}}{\frac{N_2 - B_2}{\epsilon_2}} \tag{A.2}$$

This method was first used by the CDF collaboration in 2009 to measure the cross-section for top quark pair production, with inclusive Z boson production as the second process [58]. This resulted in the most precise single measurement of the $t\bar{t}$ cross-section at the time. However, the ratio approach has a number of drawbacks. First, though the dependence of R on the integrated luminosity measurement is greatly reduced, it is not completely eliminated, as any simulation-driven background estimates entering in B_1 and B_2 will depend on the measured integrated luminosity through $B_i = \epsilon_i \sigma_i \mathcal{L}$. In the CDF analysis, the residual relative uncertainty on R due to the integrated luminosity was 0.3% — small, but not negligible. Another problem arises if the two processes result in similar final states and one wishes to estimate the background due to either process using Monte Carlo simulation. For example, in the $t\bar{t}/Z$ case, the $t\bar{t}$ background in the Z analysis is usually estimated using simulation samples. However, translating the simulation acceptance to an event yield prediction requires knowledge of the cross-section for the process, the very quantity that we hope to measure. This introduces significant complications, and one must expend additional resources to limit the amount of circularity introduced in the analysis.

The method presented here resolves these issues by combining the two cross-section analyses into a common likelihood function, in which both the cross-section for the process of interest and the integrated luminosity of the dataset are treated as parameters of interest, as shown in Equation A.3.

$$\begin{aligned} L(\sigma, \mathcal{L}, \alpha_k) \; &= \prod_i \frac{\left[S_i\left(\sigma, \mathcal{L}, \alpha_k\right) + B_i\left(\mathcal{L}, \alpha_k\right)\right]^{N_i}}{N_i!} e^{-\left[S_i(\sigma,\mathcal{L},\alpha_k)+B_i(\mathcal{L},\alpha_k)\right]} \\ &\times \prod_j \frac{\left[S_j\left(\mathcal{L}, \alpha_k\right) + B_j\left(\sigma, \mathcal{L}, \alpha_k\right)\right]^{N_j}}{N_j!} e^{-\left[S_j(\mathcal{L},\alpha_k)+B_j(\sigma,\mathcal{L},\alpha_k)\right]} \\ &\times \prod_k \frac{1}{\sqrt{2\pi}} e^{-\alpha_k^2/2} \end{aligned} \tag{A.3}$$

This has exactly the same form as Equation 6.2, but the product over analysis channels now includes both the 'signal' (i) and 'normalization' (j) cross-section analyses, and in the latter, the cross-section for the signal process is fixed to the theoretical prediction. Measurements of the cross-section for the process of interest and the integrated luminosity are simultaneously extracted by maximizing the likelihood in the two-dimensional $(\sigma, \mathcal{L})$ space. The uncertainties can be treated exactly as described in Section 6.1.

In this appendix, this method will be used to perform a measurement of the cross-section for top quark pair production in the dilepton final states. The normalization of the dataset will be obtained in-situ from an inclusive Z boson cross-section analysis. The data sample, triggers, and object selection criteria used in these analyses are identical to those used in the main text, as described in Chapter 4. The following sections describe the event selection criteria used in the two analyses, the new sources of uncertainty which affect the inclusive Z boson analysis, and the results obtained with this new technique, respectively.

A.1 Event selection

The following subsections decribe the event selection criteria used to obtain purified samples of $t\bar{t}$ and Z boson dilepton events. The two analyses share a common set of general-purpose event quality requirements: in order to reject beam background events, we require that candidates contain at least one primary vertex with at least five associated tracks and veto data events with jets resulting from out-of-time energy depositions. We also reject events with a pair of anti-aligned ($\Delta\phi > 3.10$) muons having opposite-sign impact parameters if the magnitude of each impact parameter is greater than 0.5 mm; this is done to eliminate the background from cosmic rays.

A.1.1 $t\bar{t}$ analysis

In order to obtain a purified sample of $t\bar{t}$ events, we select events containing exactly two oppositely-charged leptons. Candidate events are categorized depending on the flavour combination of the selected leptons: dielectron (ee), dimuon ($\mu\mu$), or electron-muon ($e\mu$). In the dielectron and dimuon categories, additional cuts are required to reduce the large background from $Z \to ee$ and $Z \to \mu\mu$ events, respectively. Here, we require that the invariant mass of the lepton pair $M_{\ell\ell}$ not lie within 10 GeV of the Z boson mass and that the missing transverse energy of the event be greater than 40 GeV. For electron-muon candidates, we require that the scalar sum H_{T} of the lepton and jet transverse momenta be greater than 120 GeV. Finally, in $t\bar{t}$ events, we expect to find a pair of high-p_{T} jets resulting from the hadronization of the two bottom quarks; we thus select events having at least two reconstructed jets satisfying $p_{\mathrm{T}} > 30$ GeV.

The composition of the selected sample is determined using a combination of simulation-based and data-driven techniques. The event yields expected from the $t\bar{t}$ signal and Wt, $Z \to \tau\tau$, and diboson backgrounds are obtained from the Monte Carlo simulation samples described in Section 4.2. The residual backgrounds from $Z \to ee$ and $Z \to \mu\mu$ events in the dielectron and dimuon samples are evaluated using the ABCD method (Section 5.2.1), while the background from events with one or two fake leptons is obtained from the matrix method (Section 5.2.2). The results are shown in Table A.1; 82 events are observed to pass the selection in the 2010 ATLAS dataset, consistent with the expected total of 72.6 ± 6.4. Top pair events are predicted to account for 87% of the selected sample.

Process	$e\mu$	ee	$\mu\mu$
$t\bar{t}$	37.3 ± 2.5	8.4 ± 1.2	17.8 ± 1.9
Wt	1.7 ± 0.4	0.4 ± 0.1	0.9 ± 0.2
$Z \to ee$	—	0.3 ± 0.6	—
$Z \to \mu\mu$	—	—	$1.0^{+1.8}_{-0.8}$
$Z \to \tau\tau$	2.0 ± 1.0	0.2 ± 0.2	0.9 ± 0.5
WW	0.5 ± 0.1	0.07 ± 0.02	0.15 ± 0.04
WZ	0.11 ± 0.02	0.03 ± 0.01	0.14 ± 0.04
ZZ	0.022 ± 0.004	0.011 ± 0.003	0.08 ± 0.03
Fake leptons	0.5 ± 1.0	0.1 ± 0.2	0 ± 1.3
Total background	4.8 ± 1.5	1.1 ± 0.7	$3.2^{+2.2}_{-1.5}$
Total expected	42.1 ± 3.2	9.5 ± 1.4	$21.0^{+3.1}_{-2.6}$
Observed	40	14	28

Table A.1: Expected and observed event yields in the selected $t\bar{t}$ sample. Uncertainties represent the combined effect of all statistical and systematic uncertainties as described in Chapter 6.

A.1.2 Z analysis

A purified sample of Z boson events is obtained by selecting events containing exactly two oppositely-charged electrons or muons whose invariant mass falls within 10 GeV of the Z boson mass. The orthogonality of the invariant mass requirements applied in the $t\bar{t}$ and Z analyses ensures that there is no overlap between them.

The composition of this sample is determined using a combination of simulation-based and data-driven techniques. The event yield predictions for the $Z \to ee$, $Z \to \mu\mu$, and $Z \to \tau\tau$ processes are obtained from inclusive $Z/\gamma^* \to \ell\ell$ Monte Carlo simulation samples generated with PYTHIA for the invariant mass range $M_{\ell\ell} > 60$ GeV using the MRST2007LO* PDF set, and normalized to the NNLO theoretical cross-section of 989 pb, as obtained from the FEWZ software package. The contributions from the $t\bar{t}$, Wt and diboson backgrounds are estimated from the Monte Carlo simulation samples described in Section 4.2. The background from fake leptons is estimated by assuming that, in events with one real and one fake lepton, the fake lepton has an equal probability of being positively or negatively charged, resulting in equal probabilities for opposite-charge and same-charge events. The number of same-charge data events passing the event selection is thus taken as the event yield prediction for the fake lepton background.

The results are shown in Table A.2. 4,977 (12,313) dielectron (dimuon) events are observed to pass the selection in the 2010 ATLAS dataset, consistent with the expected total of $4,913 \pm 450$ ($12,269 \pm 900$). The Z purity of both samples is predicted to be greater than 99%.

A.2 Uncertainties

All sources of uncertainty discussed in Chapter 6 are taken into account in both cross-section analyses, with the exception of the integrated luminosity, which is treated as a free parameter in this method. Correlations between the two analyses are also treated

Process	ee	$\mu\mu$
$t\bar{t}$	2.3 ± 0.4	5.4 ± 0.9
Wt	0.21 ± 0.04	0.6 ± 0.1
$Z \rightarrow ee$	$4,899 \pm 450$	—
$Z \rightarrow \mu\mu$	—	$12,247 \pm 898$
$Z \rightarrow \tau\tau$	0.2 ± 0.1	1.6 ± 0.3
WW	0.6 ± 0.1	1.4 ± 0.1
WZ	3.1 ± 0.3	7.2 ± 0.5
ZZ	2.5 ± 0.2	5.7 ± 0.4
Fake leptons	6 ± 6.5	0 ± 1.4
Total background	15 ± 7	22 ± 2
Total expected	$4,913 \pm 450$	$12,269 \pm 900$
Observed	4977	12313

Table A.2: Expected and observed event yields in the selected Z sample. Uncertainties represent the combined effect of all statistical and systematic uncertainties as described in Chapter 6 and Section A.2.

appropriately — for example, raising the muon energy scale might increase the dimuon invariant mass of a simulated $t\bar{t}$ dimuon event from 79 to 83 GeV, causing it to go from a signal event in the $t\bar{t}$ analysis to a background event in the inclusive Z analysis.

Wt-channel single top quark production is a background to both of the analyses discussed in this appendix. The event yields for this process are normalized using the NLO theoretical cross-section shown in Table 4.1; a 10% relative uncertainty is associated to this value and treated as fully correlated with the other background cross-section uncertainties.

In the inclusive Z boson cross-section analysis, the theoretical cross-section for inclusive Z production is used to convert the acceptance obtained from the simulation sample to a predicted number of events per unit of integrated luminosity. This parameter has an uncertainty of 5% [59], which includes the contributions from the α_S uncertainty, electroweak corrections, scale variations, and parton density functions. The uncertainty on the inclusive Z boson acceptance from the choice of generator and parton shower model is evaluated by comparing the nominal acceptance with that obtained from a MC@NLO/HERWIG sample, resulting in a 2.8% effect [60]. The acceptance uncertainty for inclusive Z boson events stemming from the choice of PDF set and the errors within each PDF set were also evaluated and amount to 2.6% [60].

A.3 Results

The expected and observed profile likelihood ratio contours are shown in Figure A.1. Accounting for all sources of statistical and systematic uncertainty, we measure the cross-section for top quark pair production to be

$$\sigma(pp \to t\bar{t}) = 188\ ^{+21}_{-19}\ (\text{stat})\ ^{+4}_{-19}\ (\text{syst})\ \text{pb}.$$

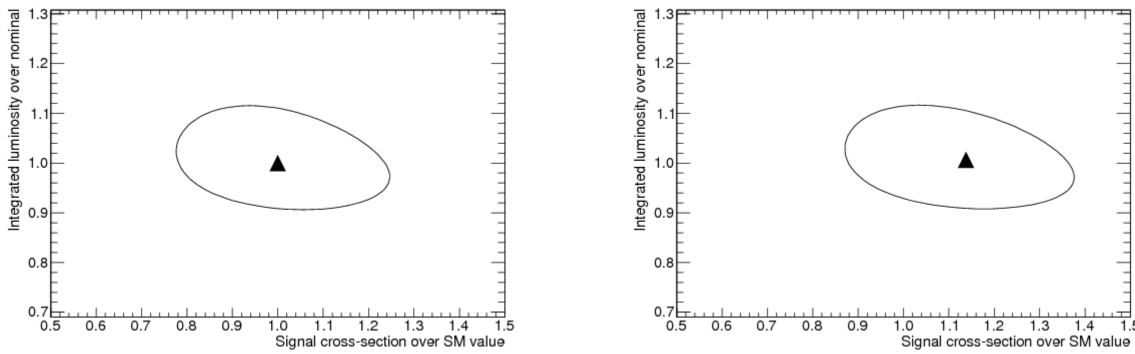

Figure A.1: Expected (left) and observed (right) 1σ profile likelihood contours in the $(\sigma_{t\bar{t}}, \mathcal{L})$ plane. The triangle marker denotes the position of the maximum likelihood estimate.

We also extract the following measurement for the integrated luminosity of the 2010 ATLAS dataset:

$$\mathcal{L} = 35.3 \ \pm 0.3\,(\text{stat}) \ \pm 2.4\,(\text{syst})\ \text{pb}^{-1}.$$

The full breakdown of the uncertainty on both expected measurements is provided in Table A.3, and is also contrasted with the performance of a 'standard' $t\bar{t}$ cross-section analysis in which the event yields are normalized using the experimentally measured integrated luminosity of the dataset. Despite the fact that this method effectively replaces a 3.4% systematic uncertainty ($\mathcal{L}$) with a 5-7% uncertainty (inclusive Z cross-section + modeling), the analysis employing in-situ Z boson normalization performs slightly better overall. This is due to the fact that the effect of any sources of systematic uncertainty which are correlated between the $t\bar{t}$ and Z analyses will partially cancel out in the combination, as can be seen most obviously with the lepton performance uncertainties.

Source	$\Delta\sigma/\sigma$ [%]	$\Delta\sigma/\sigma$ [%]	$\Delta\mathcal{L}/\mathcal{L}$ [%]
Data statistics	+14.0/-12.9	+13.9/-12.9	+0.8/-0.8
MC statistics	+2.0/-2.1	+1.8/-2.0	+0.1/-0.1
Luminosity	+4.0/-3.6	—	—
Electron performance	+3.7/-3.1	+0.8/-0.6	+0.5/-0.5
Muon performance	+0.5/-0.7	+0.3/-0.2	+0.5/-0.6
Jet performance	+4.3/-4.6	+4.5/-4.7	+0.3/-0.2
$E_{\mathrm{T}}^{\mathrm{miss}}$ performance	+0.0/-0.5	+0.1/-0.2	+0.0/-0.0
$Z \to \ell\ell$ background estimation	+1.2/-2.9	+1.2/-2.9	+0.0/-0.0
Fake lepton background estimation	+0.9/-4.0	+1.2/-3.9	+0.0/-0.0
Theoretical cross-sections	+2.2/-2.7	+3.8/-2.7	+4.7/-4.5
Generator choice	+3.4/-3.4	+3.3/-2.6	+2.7/-2.6
Initial/final state radiation	+0.7/-0.0	+0.7/-0.0	+0.0/-0.0
Parton distribution functions	+2.3/-2.0	+0.8/-0.7	+0.4/-0.4
All systematics	+9.3/-9.2	+7.5/-7.9	+7.3/-6.3
Total uncertainty	+16.7/-15.9	+15.8/-15.1	+7.3/-6.4

Table A.3: Breakdown of the relative uncertainties on the expected $t\bar{t}$ cross-section and integrated luminosity measurements. The second column shows the expected top pair cross-section result from a 'standard' analysis, in which the event yields are normalized using $\mathcal{L} = 35 \pm 1$ pb^{-1}.

Bibliography

[1] CDF Collaboration, F. Abe et al., *Observation of top quark production in $\bar{p}p$ collisions*, Phys. Rev. Lett. **74** (1995) 2626–2631, arXiv:hep-ex/9503002.

[2] D0 Collaboration, S. Abachi et al., *Observation of the top quark*, Phys. Rev. Lett. **74** (1995) 2632–2637, arXiv:hep-ex/9503003.

[3] CDF Collaboration, T. Aaltonen et al., *Evidence for a Mass Dependent Forward-Backward Asymmetry in Top Quark Pair Production*, Phys. Rev. **D83** (2011) 112003, arXiv:1101.0034 [hep-ex].

[4] D0 Collaboration, V. M. Abazov et al., *Observation of Single Top-Quark Production*, Phys. Rev. Lett. **103** (2009) 092001, arXiv:0903.0850 [hep-ex].

[5] CDF Collaboration, T. Aaltonen et al., *Observation of Electroweak Single Top-Quark Production*, Phys. Rev. Lett. **103** (2009) no. 9, 092002, arXiv:0903.0885 [hep-ex].

[6] D0 Collaboration, V. Abazov et al., *Measurement of the t-channel single top quark production cross section*, Phys. Lett. **B682** (2010) no. 4-5, 363 – 369, arXiv:0907.4259 [hep-ex].

[7] ATLAS Collaboration, G. Aad et al., *Expected Performance of the ATLAS Experiment - Detector, Trigger and Physics*, arXiv:0901.0512 [hep-ex].

[8] ATLAS Collaboration, *Prospects for associated single top quark production cross-section measurements in the dilepton decay mode with ATLAS*, ATL-PHYS-PUB-2009-001.

[9] CMS Collaboration, G. L. Bayatian et al., *CMS physics Technical Design Report, Volume II: Physics Performance*, J. Phys. **G34** (2006) 995–1579.

[10] CMS Collaboration, *Prospects for the measurement of the single-top t-channel cross section in the muon channel with 200 pb*$^{-1}$, CMS-PAS-TOP-09-005.

[11] S. L. Glashow, *Partial Symmetries of Weak Interactions*, Nucl. Phys. **22** (1961) 579–588.

[12] S. Weinberg, *A Model of Leptons*, Phys. Rev. Lett. **19** (1967) 1264–1266.

[13] A. Salam, *Weak and Electromagnetic Interactions*, originally printed in Svartholm: Elementary Particle Theory, Proceedings Of The Nobel Symposium Held 1968 At Lerum, Sweden, Stockholm 1968, 367-377.

[14] S. L. Glashow, J. Iliopoulos, and L. Maiani, *Weak Interactions with Lepton-Hadron Symmetry*, Phys. Rev. **D2** (1970) 1285–1292.

[15] P. W. Higgs, *Broken symmetries, massless particles and gauge fields*, Phys. Lett. **12** (1964) 132–133.

[16] P. W. Higgs, *Spontaneous Symmetry Breakdown without Massless Bosons*, Phys. Rev. **145** (1966) 1156–1163.

[17] F. Englert and R. Brout, *Broken Symmetry And the Mass of Gauge Vector Mesons*, Phys. Rev. Lett. **13** (1964) 321–322.

[18] G. S. Guralnik, C. R. Hagen, and T. W. B. Kibble, *Global Conservation Laws And Massless Particles*, Phys. Rev. Lett. **13** (1964) 585–587.

[19] Particle Data Group Collaboration, K. Nakamura et al., *Review of particle physics*, J. Phys. **G37** (2010) 075021.

[20] M. Aliev et al., *– HATHOR – HAdronic Top and Heavy quarks crOss section calculatoR*, Comput. Phys. Commun. **182** (2011) 1034–1046, arXiv:1007.1327 [hep-ph].

[21] N. Kidonakis, *Next-to-next-to-leading-order collinear and soft gluon corrections for t-channel single top quark production*, Phys. Rev. **D83** (2011) 091503, arXiv:1103.2792 [hep-ph].

[22] N. Kidonakis, *Two-loop soft anomalous dimensions for single top quark associated production with a W- or H-*, Phys. Rev. **D82** (2010) 054018, arXiv:1005.4451 [hep-ph].

[23] N. Kidonakis, *NNLL resummation for s-channel single top quark production*, Phys. Rev. **D81** (2010) 054028, arXiv:1001.5034 [hep-ph].

[24] W. Bernreuther, *Top quark physics at the LHC*, J. Phys. **G35** (2008) 083001, arXiv:0805.1333 [hep-ph].

[25] T. M. P. Tait and C. P. Yuan, *Single Top Production as a Window to Physics Beyond the Standard Model*, Phys. Rev. **D63** (2001) 014018, arXiv:hep-ph/0007298.

[26] O. Eberhardt, A. Lenz, and J. Rohrwild, *Less space for a new family of fermions*, Phys. Rev. **D82** (2010) 095006, arXiv:1005.3505 [hep-ph].

[27] O. S. Bruning, (Ed.) et al., *LHC design report. Vol. I: The LHC main ring*, CERN-2004-003-V-1.

[28] O. Buning, (Ed.) et al., *LHC Design Report. Vol. II: The LHC infrastructure and general services*, CERN-2004-003-V-2.

[29] M. Benedikt, (Ed.), P. Collier, (Ed.), V. Mertens, (Ed.), J. Poole, (Ed.), and K. Schindl, (Ed.), *LHC Design Report. Vol. III: The LHC injector chain*, CERN-2004-003-V-3.

[30] ATLAS Collaboration, G. Aad et al., *The ATLAS Experiment at the CERN Large Hadron Collider*, JINST **3** (2008) S08003.

[31] S. Frixione and B. R. Webber, *The MC@NLO 3.4 Event Generator*, arXiv:0812.0770 [hep-ph].

[32] S. Frixione, E. Laenen, P. Motylinski, B. R. Webber, and C. D. White, *Single-top hadroproduction in association with a W boson*, JHEP **07** (2008) 029, arXiv:0805.3067 [hep-ph].

[33] M. L. Mangano, M. Moretti, F. Piccinini, R. Pittau, and A. D. Polosa, *ALPGEN, a generator for hard multiparton processes in hadronic collisions*, JHEP **07** (2003) 001, arXiv:hep-ph/0206293.

[34] C. Anastasiou, L. J. Dixon, K. Melnikov, and F. Petriello, *High precision QCD at hadron colliders: Electroweak gauge boson rapidity distributions at NNLO*, Phys. Rev. **D69** (2004) 094008, arXiv:hep-ph/0312266.

[35] G. Corcella et al., *HERWIG 6.5: an event generator for Hadron Emission Reactions With Interfering Gluons (including supersymmetric processes)*, JHEP **01** (2001) 010, arXiv:hep-ph/0011363.

[36] J. M. Campbell and R. K. Ellis, *Radiative corrections to Z b anti-b production*, Phys. Rev. **D62** (2000) 114012, arXiv:hep-ph/0006304.

[37] P. M. Nadolsky et al., *Implications of CTEQ global analysis for collider observables*, Phys. Rev. **D78** (2008) 013004, arXiv:0802.0007 [hep-ph].

[38] J. Pumplin et al., *New generation of parton distributions with uncertainties from global QCD analysis*, JHEP **07** (2002) 012, arXiv:hep-ph/0201195.

[39] A. Sherstnev and R. S. Thorne, *Parton Distributions for LO Generators*, Eur. Phys. J. **C55** (2008) 553–575, arXiv:0711.2473 [hep-ph].

[40] J. M. Butterworth, J. R. Forshaw, and M. H. Seymour, *Multiparton interactions in photoproduction at HERA*, Z. Phys. **C72** (1996) 637–646, arXiv:hep-ph/9601371.

[41] ATLAS Collaboration, *First tuning of HERWIG/JIMMY to ATLAS data*, ATL-COM-PHYS-2010-620.

[42] ATLAS Collaboration, G. Aad et al., *The ATLAS Simulation Infrastructure*, Eur. Phys. J. **C70** (2010) 823–874, arXiv:1005.4568 [physics.ins-det].

[43] GEANT4 Collaboration, S. Agostinelli et al., *GEANT4: A simulation toolkit*, Nucl. Instrum. Meth. A **506** (2003) 250–303.

[44] M. Cacciari, G. P. Salam, and G. Soyez, *The anti-k_t jet clustering algorithm*, JHEP **04** (2008) 063, arXiv:0802.1189 [hep-ph].

[45] ATLAS Collaboration, G. Aad et al., *Luminosity Determination in pp Collisions at $\sqrt{s} = 7$ TeV Using the ATLAS Detector at the LHC*, Eur. Phys. J. **C71** (2011) 1630, arXiv:1101.2185 [hep-ex].

[46] ATLAS Collaboration, *Updated Luminosity Determination in pp Collisions at $\sqrt{s} = 7$ TeV using the ATLAS Detector*, ATLAS-CONF-2011-011.

[47] ATLAS Collaboration, *Reconstruction and Calibration of Missing Transverse Energy and Performance in Z and W events in ATLAS Proton-Proton Collisions at 7 TeV*, ATLAS-CONF-2011-080.

[48] J. Alwall et al., *Comparative study of various algorithms for the merging of parton showers and matrix elements in hadronic collisions*, Eur. Phys. J. **C53** (2008) 473–500, `arXiv:0706.2569 [hep-ph]`.

[49] P. Nason, *A new method for combining NLO QCD with shower Monte Carlo algorithms*, JHEP **11** (2004) 040, `arXiv:hep-ph/0409146`.

[50] S. Frixione, P. Nason, and C. Oleari, *Matching NLO QCD computations with Parton Shower simulations: the POWHEG method*, JHEP **11** (2007) 070, `arXiv:0709.2092 [hep-ph]`.

[51] S. Alioli, P. Nason, C. Oleari, and E. Re, *A general framework for implementing NLO calculations in shower Monte Carlo programs: the POWHEG BOX*, JHEP **06** (2010) 043, `arXiv:1002.2581 [hep-ph]`.

[52] T. Sjostrand, S. Mrenna, and P. Z. Skands, *PYTHIA 6.4 Physics and Manual*, JHEP **05** (2006) 026, `arXiv:hep-ph/0603175`.

[53] B. P. Kersevan and E. Richter-Was, *The Monte Carlo event generator AcerMC version 2.0 with interfaces to PYTHIA 6.2 and HERWIG 6.5*, `arXiv:hep-ph/0405247`.

[54] A. D. Martin, W. J. Stirling, R. S. Thorne, and G. Watt, *Parton distributions for the LHC*, Eur. Phys. J. **C63** (2009) 189–285, `arXiv:0901.0002 [hep-ph]`.

[55] R. D. Ball et al., *A first unbiased global NLO determination of parton distributions and their uncertainties*, Nucl. Phys. **B838** (2010) 136–206, `arXiv:1002.4407 [hep-ph]`.

[56] G. Cowan, K. Cranmer, E. Gross, and O. Vitells, *Asymptotic formulae for likelihood-based tests of new physics*, Eur. Phys. J. **C71** (2011) 1554, `arXiv:1007.1727 [hep-ex]`.

[57] ATLAS Collaboration, W. W. Armstrong et al., *ATLAS: Technical proposal for a general-purpose pp experiment at the Large Hadron Collider at CERN*, CERN-LHCC-94-43.

[58] CDF Collaboration, T. Aaltonen et al., *First Measurement of the Ratio* $\sigma_{t\bar{t}}/\sigma_{Z/\gamma^* \to \ell\ell}$ *and Precise Extraction of the* $t\bar{t}$ *Cross Section*, Phys. Rev. Lett. **105** (2010) 012001, arXiv:1004.3224 [hep-ex].

[59] J. Butterworth, E. Dobson, U. Klein, B. M. Garcia, T. Nunnemann, J. Qian, D. Rebuzzi, and R. Tanaka, *Single Boson and Diboson Production Cross Sections in pp Collisions at* $\sqrt{s} = 7$ *TeV*, ATLAS-COM-PHYS-2010-695.

[60] M. Schott, D. Froideveaux, and M. Boonekamp, *Total inclusive* W *and* Z *boson cross-section measurements, cross-section ratios and combinations in the electron and muon decay channels at 7 TeV based on 300* nb^{-1}, ATLAS-COM-PHYS-2010-703.